Orbital (Hydro)Climate Variability in the Ice-Free early Eocene Arctic

Chris D. Fokkema[1]*, Henk Brinkhuis[1,2], Francien Peterse[1] and Appy Sluijs[1]

[1] Department of Earth Sciences, Faculty of Geoscience, Utrecht University, 3584CB Utrecht, The Netherlands

[2] Royal Netherlands Institute for Sea Research (NIOZ), 1790 AB Den Burg, The Netherlands.

*Corresponding author: Chris D. Fokkema (c.d.fokkema@uu.nl)

Key Points:

- TEX_{86}-based early Eocene Arctic surface water temperatures (SSTs) depict obliquity and precession imprints suggestive of a spring-to-fall forcing.
- Eccentricity forcing caused ~0.8 °C Arctic SST variability, showing strong Arctic amplification despite absent albedo feedbacks.
- Precipitation maxima were in-phase with implied insolation maxima, suggesting a strong orbital imprint on local hydrological processes.

Abstract

We explore the imprint of orbital variability on Arctic temperature and hydrology using sediments recovered during the Arctic Coring Expedition in 2004. High resolution records of lipid biomarkers (GDGTs; 2-kyr) and palynological assemblages (5-kyr) in the ~4 m interval below Eocene Thermal Maximum 2 (~54 Ma) show highly cyclic signals related to ~20-kyr precession, ~40-kyr obliquity and ~100-kyr eccentricity. The GDGTs indicate obliquity and precession variability representative of sea surface temperature (SST) variations up to ~1.4 and ~0.5 ºC, respectively. Peak SSTs coincide with an elevated supply of pollen and spores and increased marine productivity. Together, this implies an orbital control on precipitation and terrestrial nutrient supply to the Arctic Basin. Assuming that SST maxima correspond to Arctic insolation maxima (precession minima/obliquity maxima), precipitation maxima also correspond to insolation maxima, implying regional hydrological processes as a forcing rather than variations in meridional water transport, starkly contrasting Pleistocene Arctic hydrology. The relative amplitudes of precession and obliquity in the SST record match that of local insolation between spring and fall, corroborating previous suggestions of a seasonal GDGT bias. The reconstructed complete orbital imprint refutes that ACEX temperature reconstructions are biased to one end of the orbital variability. Eccentricity-related SST variability was ~0.8 ºC, ~2–3 times higher than synchronous variability in the deep ocean, and 3–4 times higher than similar variations in the tropics. This confirms eccentricity-forced global temperature variability during the Eocene, and that this had pronounced polar amplification, despite the absence of ice and snow albedo feedbacks.

Plain Language Summary

During the early Eocene (56–48 million years ago), an ancient period of global high atmospheric CO_2 concentrations and temperatures, the Arctic Ocean was an ice-free, (sub)tropical, semi-enclosed basin. Our understanding of this unfamiliar Arctic situation relies largely on geochemical and (micro)fossil analysis of sediments retrieved by the single academic drilling expedition that recovered sediments from this period. However, the available temperature data of the Eocene Arctic are insufficient to capture the climate variations caused by Earth's orbit (often termed "Milankovitch cycles"), which are also responsible for the repeating occurrence of ice ages over the past million years. Here, we reconstruct past Arctic temperatures using temperature-sensitive molecular fossils in a 4-m thick sediment interval deposited during the early Eocene on a 1-cm (~2,000-year) resolution. Our results show that Arctic surface temperatures varied more than those at lower latitudes during global variations, and display 2 ºC variability corresponding to the local insolation changes resulting from precession and the tilt of Earth's axis, with respective periods of 21,000 and 41,000 years. Changes in microfossil content show that the warmer periods coincided with increased rainfall, indicating that moisture availability at the poles was similarly forced on these timescales.

1 Introduction

Millennial-scale fluctuations of insolation induced by Earth's orbital parameters (i.e., Milankovitch cycles) are at their extremes at the poles, where obliquity forces changes up to ~10% (~34 W/m^2) of the annual average insolation, and precession up to ~20% (~80 W/m^2) in peak summer insolation (Laskar et al., 2004; Li et al., 2019). These Milankovitch variations — also including orbital eccentricity that modulates the amplitude of precession — at the high latitudes were responsible for the pacing of glacial-interglacial variability since the establishment of a more permanent cryosphere at the Oligocene-Eocene transition (e.g.,Westerhold et al., 2020). In the Pleistocene, their regional impact on the sea surface temperature (SST) of the Arctic Ocean was strongly reduced due to the high albedo and insulation of the sea ice cover, and clipped at minimum SSTs of approximately -2 °C (e.g., Carton et al., 2015). Hypothetically, the imprint of orbital forcing on Arctic SST is expected to be much larger in the absence of (sea)ice during past "hothouse" climates. Furthermore, because the poles experience the maximum seasonality of insolation — daily insolation at the poles ranges from zero in winter to values exceeding tropical insolation in summer — an ice-free pole would imply a non-analog climate state that experiences extreme seasonal SST variability.

The presence of significant ice sheets can be ruled out for the early Eocene (~56–48 Ma), characterized by high atmospheric pCO_2 (Anagnostou et al., 2020) and high global mean temperatures (Inglis et al., 2020). Overall warm climate in the early Eocene was accentuated by multiple transient global warming events (“hyperthermals”), of which the Paleocene-Eocene Thermal Maximum (PETM; 56 Ma (Kennett and Stott, 1991; Zachos et al., 2003; Sluijs et al., 2006)) and Eocene Thermal Maximum 2 (ETM2; 54 Ma (Lourens et al., 2005; Sluijs et al., 2009)) are best known. These events are globally marked by negative stable carbon isotope ($\delta^{13}C$) excursions (CIEs) in organic and inorganic sedimentary components and deep ocean acidification due to the release of ^{13}C-depleted carbon into the ocean-atmosphere system (Dickens et al., 1995, 1997). The pattern and occurrence of these CIEs, as well as long-term $\delta^{13}C$ trends, combined with biostratigraphy, have proven to be excellent stratigraphic correlation tools, which can be used to compare climatic variations associated with hyperthermals on global scales (e.g., Cramer et al., 2003; Westerhold et al., 2018; Fokkema et al., 2023), and have been used to prove that most, if not all, occur during maxima in the eccentricity of Earth’s orbit (Lourens et al., 2005; Galeotti et al., 2010; Lauretano et al., 2018).

Of key importance to understanding Paleogene climate and its hyperthermals has been the Integrated Ocean Drilling Program (IODP) Expedition 302 in 2004, also known as the Arctic Coring Expedition (ACEX). At IODP Site M0004 (paleolatitude 78º N, Fig. 1), ACEX recovered an uppermost Paleocene to lower Eocene sequence comprised of organic-rich siliciclastic mudstone from the Lomonosov Ridge (Backman et al., 2006). While the Paleogene sediments are barren of calcareous and siliceous microfossils, they proved to be rich in lipid biomarkers and palynomorphs (Backman et al., 2006). By combined organic walled dinoflagellate cyst (dinocyst) biostratigraphy and $\delta^{13}C$-chemostratigraphy, two CIEs (~384 meters composite depth (mcd), Core 30X and ~369 mcd, Core 27X, respectively) were identified as the PETM and ETM2 hyperthermal events (Stein et al., 2006; Sluijs et al., 2006, 2009).

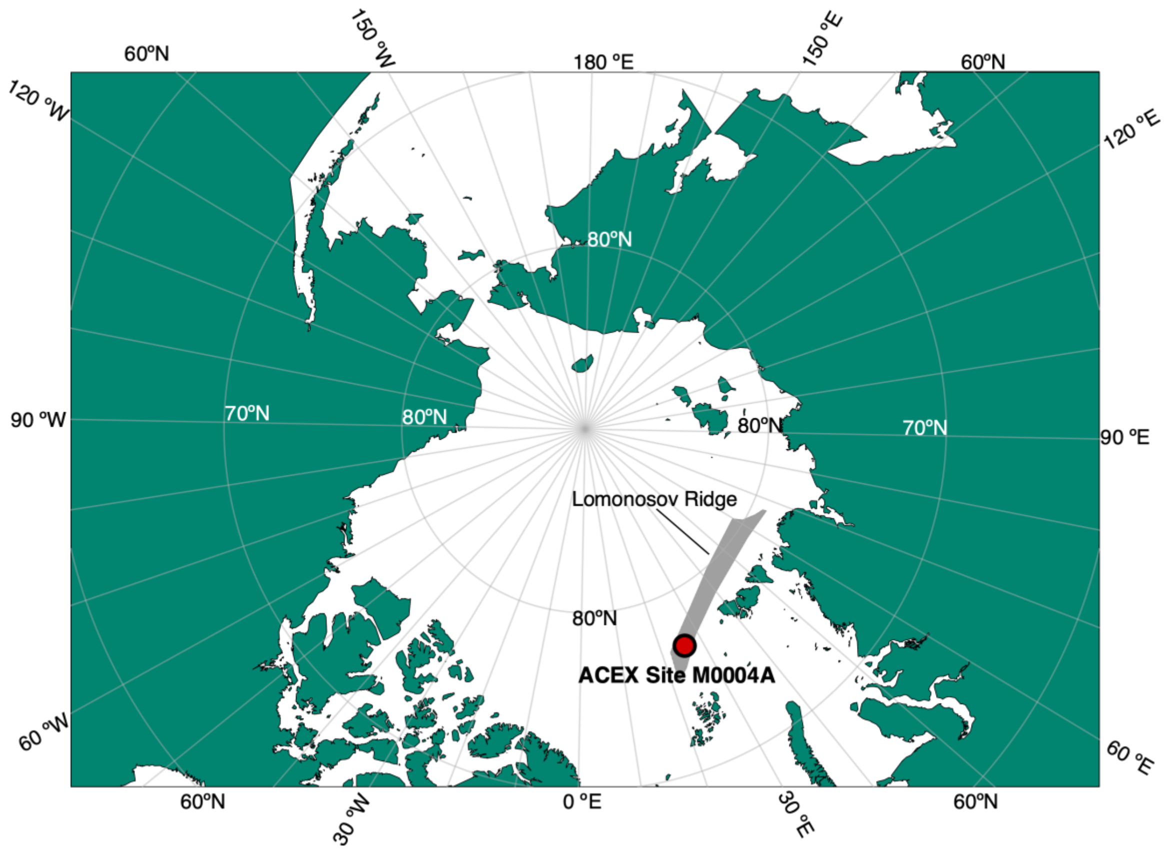

Figure 1. Paleogeographic map showing the position of ACEX Site M0004A (red dot) in the early Eocene Arctic Ocean on Lomonosov Ridge (grey area). Figure adapted from (Sluijs et al. (2020).

The TetraEther indeX of 86 carbon atoms (TEX_{86}) is a water temperature proxy based on the number of cyclic moieties in Nitrososphaeral (previously named "Thaumarchaeota" or "Crenarchaeota") membrane lipids termed glycerol dialkyl glycerol tetraethers (GDGTs) (Schouten et al., 2002). Application of this molecular paleothermometer at Site M0004A has revealed anomalously high Arctic SSTs exceeding 20 °C and reaching temperatures as high as 26 °C and 27 °C during peak PETM and ETM2 (Sluijs et al., 2006, 2008b, 2009, 2020). Furthermore, these warming phases appeared associated with drastic environmental change. For example, the warming during both PETM and ETM2 led to wetter conditions in the Arctic, evidenced by increased low-salinity tolerant dinocysts and reduced proportions of terrestrial palynomorphs (Sluijs et al., 2006, 2008a, 2009). Accordingly, changes in the hydrogen isotope composition of plant waxes indicated increased poleward moisture transport during the hyperthermals that could have facilitated this increased rainfall (Pagani et al., 2006; Krishnan et al., 2014). Coeval presence of isorenieratene, a biomarker exclusively produced by green sulfur bacteria, points to photic zone euxinia, a consequence of enhanced freshwater stratification, warming and elevated terrestrial nutrient input in the basin (Sluijs et al., 2006, 2009). On land, the environmental extremes favored occurrence of megathermal floral taxa, including palms and even tropical baobab trees (Sluijs et al., 2009; Willard et al., 2019). These hydrological changes were not unique to the Lomonosov Ridge margin, but a widespread Arctic phenomena, given evidence from the, albeit nearby, Arctic Siberian margin (Suan et al., 2017).

The non-analog temperatures of the early Eocene Arctic region as well as the southern high latitudes are historically problematic for climate models to explain under realistic CO_2 concentrations and/or meridional gradients, not only at the time of the early publications (e.g., Sluijs et al., 2006; Bijl et al., 2009), but even with the current state-of-the-art fully coupled climate models (e.g., Evans et al., 2018; Cramwinckel et al., 2018; Lunt et al., 2021). Also hydrological patterns appear challenging to simulate in accordance with proxy data (Cramwinckel et al., 2023). However, the expected high amplitude of orbital climate variability in an ice-free Arctic may imply that the existing (low-resolution) proxy records either represent aliased climate signals, or climate signals that are biased towards one extreme of the variability. For instance, sedimentation might have been biased towards the orbital configurations that led to highest siliciclastic sediment supply, for which reconstruction of the complete orbital cycle would potentially provide a less biased reconstruction of the climate signals. Moreover, while TEX_{86} is generally considered a proxy for mean annual SSTs, it was suggested that the export of lipid biomarkers through fecal pelleting may have been biased towards the summer season (Sluijs et al., 2006, 2020). Many of these concerns can be tested with higher-resolution reconstructions, especially if orbital variability can be resolved. The patterns of orbital forcing on insolation are characteristic per season and duration of the forcing (Fig. 2). For example, absence of precession forcing in a climate parameter would imply a true annually averaged signal, while absence of obliquity occurs during the equinoxes. Hence, the reconstruction of orbital cyclicity in SST variations at the Lomonosov Ridge could help to put constrains on both the problem of orbital clipping and seasonality of the signal.

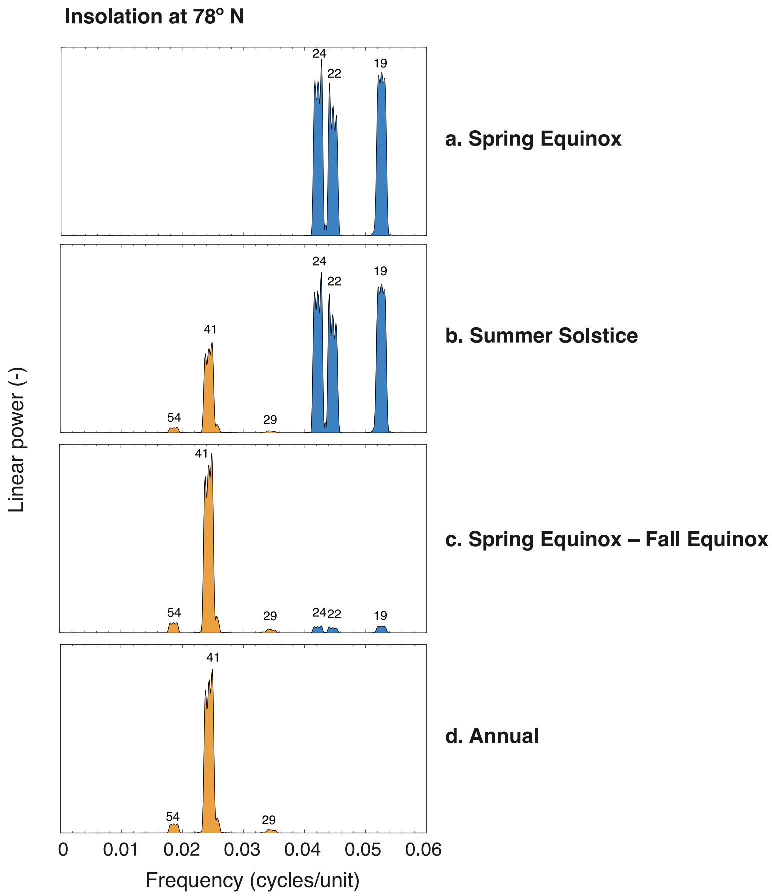

Figure 2. Power spectra of insolation at 78 ° N, showing obliquity (orange) and precession (blue) frequencies. (**a**) Insolation spectra during the spring equinox (~21 March). (**b**) Insolation spectra during the summer solstice (~21 June). (**c**) Averaged insolation spectra between the spring and fall equinoxes (~21 March – 22 September). (**d**) Mean annual averaged insolation spectra. All spectra are calculated using the Multitaper Method in Acycle (Li et al., 2019) over insolation curves for the past two million years (Laskar et al., 2004). Numbers above spectral peaks indicate the corresponding periods in kyrs.

Previous work on the ACEX sediments has identified orbitally forced patterns in Paleogene sediments at the Lomonosov Ridge, including in the physical and geochemical sediment properties (Sangiorgi et al., 2008; Pälike et al., 2008; Sluijs et al., 2008b), as well as palynomorph assemblages (Sangiorgi et al., 2008; Barke et al., 2011). This work has shown that sedimentation on the Lomonosov Ridge margin was significantly affected by climatic precession and obliquity, likely mainly due to regional (hydro)climatic variability. Decimeter scale variations in color and iron content in a laminated section, just below the ETM2 interval, have been interpreted as precession and obliquity cycles (Sluijs et al., 2008b). However, apart from XRF-based lithological indicators, the current environmental proxy data are of insufficient temporal resolution to capture this orbital variability to its fullest and resolve any environmental variability on these timescales.

Therefore, we here present the first high-resolution analyses of IODP Site M0004A Core 27X across the largely laminated interval covering ETM2 and the cyclic sediments below it (~372–367.8 mcd). By utilizing combined lipid biomarkers and palynological datasets, we (1) aim to detect the imprint of Milankovitch cycles on Arctic climate, (2) provide a quantitative estimate of SST variability associated with the recorded orbital cycles using TEX_{86}, and (3) provide a qualitative assessment of the hydrological change coupled to the temperature change by assessing the abundance of terrestrial biomarkers and palynomorphs and low-salinity tolerant dinocysts.

2 Materials and Methods

2.1 Site and sampling

Previous work on the ACEX sediments has identified orbitally forced patterns in Paleogene sediments at the Lomonosov Ridge, including in the physical and geochemical sediment properties (Sangiorgi et al., 2008; Pälike et al., 2008; Sluijs et al., 2008b), as well as palynomorph assemblages (Sangiorgi et al., 2008; Barke et al., 2011). This work has shown that sedimentation on the Lomonosov Ridge margin was significantly affected by climatic precession and obliquity, likely mainly due to regional (hydro)climatic variability. Decimeter scale variations in color and iron content in a laminated section, just below the ETM2 interval, have been interpreted as precession and obliquity cycles (Sluijs et al., 2008b). However, apart from XRF-based lithological indicators, the current environmental proxy data are of insufficient temporal resolution to capture this orbital variability to its fullest and resolve any environmental variability on these timescales.

2.2 Magnetic susceptibility

As a first order estimate of the iron content, magnetic susceptibility was measured on each sample. For this, samples were first weighed in and measured for bulk magnetic susceptibility, using a MFKF1-FA, with a precision better than 3.87×10^{-8} χ.

2.3 Color analysis

High-resolution line-scan photographs (10 pixels/mm) of the archive halves (Backman et al., 2006) were used to generate sediment color logs. For this, first, the cracks were removed using the "DeCrack" program (Zeeden et al., 2015). Next, all remaining post-depositional features were removed from the core pictures (e.g., bioturbation, secondary mineral phases, drilling mud) using photo editing software. Finally, mean greyscale values were calculated on a 1 cm resolution with the "Colourlog" R-script (Kocken, 2022).

2.4 Lipid biomarkers

2.4.1 Lipid biomarker analysis

For the lipid biomarker analysis, on average 2 grams (ranging from 0.4 to 6.4 grams) of powdered and homogenized sediment was extracted with 25 ml dichloromethane (DCM):MeOH (9:1 v/v), using a Milestone Ethos X Microwave Extraction System for 50 minutes at 70 ºC. A known amount of C_{46} glycerol trialkyl glycerol tetraether (GTGT) standard was added to each lipid extract. The extracts were then passed over a NaO_2 column to remove any remaining water, and dried under a gentle N_2 stream. The lipid extract was separated in an apolar, ketone and polar fraction over an activated Al_2O_3 column, utilizing hexane:DCM (9:1), hexane:DCM (1:1) and 1:1 DCM:MeOH (1:1) as respective solvents. For GDGT analysis, the polar fraction was first dried under N_2, and then redissolved in 99:1 hexane:isopropanol, filtered through a 0.45 μm polytetrafluoroethylene filter and injected into an Agilent 1290 infinity ultra high-performance liquid chromatograph (UHPLC) coupled to an Agilent 6135 single quadrupole mass spectrometer using the method and instrument settings of Hopmans et al. (2016). Isoprenoid GDGTs (isoGDGTs) and branched GDGTS (brGDGTs) were identified using selected ion monitoring (SIM) mode based on the detection of the $[M+H]^+$ ions, maintaining an integrated peak area of >2000 and a signal-to-noise ratio of >3 as detection limit. An in-house GDGT standard was injected ~every 10 samples to trace stability of the system, and provide control on analytical uncertainty.

A set of samples within one interval of low GDGT concentrations (371.035–371.565 mcd) were pooled with neighboring samples to achieve the required amount of GDGTs for appropriate signal-to-noise ratios, resulting in 11 pooled sample intervals of 2 cm representing between 2.3 and 9.8 grams of extracted sediment.

2.4.2 GDGT-based proxies

We reconstructed temperatures using the isoGDGT-based TEX_{86} paleothermometer (Equation 1). IsoGDGTs in marine sediments are predominantly produced by shallow-subsurface-ocean (~50–200 m) dwelling Nitrososphaerales (Massana et al., 2000; Sinninghe Damsté et al., 2002; Schouten et al., 2002; Hurley et al., 2018). However, sedimentary isoGDGTs potentially contain significant contributions of other sources, e.g., from terrestrial, deeper-marine, methanotrophic, methanogenic or anaerobic methane oxidizing archaea communities, which can compromise the TEX_{86} - temperature relationship (Hopmans et al., 2004; Blaga et al., 2009; Zhang et al., 2011, 2016; Weijers et al., 2011; Taylor et al., 2013). Therefore, all data were tested for such contributions by several published indices and ratios using the R-script from Bijl et al. (2021) before further implementation of TEX_{86} paleothermometry.

$$TEX_{86} = \frac{isoGDGT-2 + isoGDGT-3 + cren'}{isoGDGT-1 + isoGDGT-2 + isoGDGT-3 + cren'} \quad (1)$$

TEX_{86} values were translated to shallow subsurface temperatures at a 100–250 m depth range ($SubT_{100-250}$), following the calibration by Ho and Laepple (2016) to track the temperature variability in the niche of Nitrososphaerales in the water column. Importantly, the general one-to-one covariance of shallow SubTs and SSTs, for instance depicted by models, legitimizes reconstruction of SST variability through shallow SubT reconstructions (Ho and Laepple, 2016; Fokkema et al., 2023). Additionally, we estimated absolute SSTs using the TEX_{86}^H calibration, which calibrates GDGTs in a global surface sediment dataset to satellite-based surface ocean temperatures (Kim et al., 2010). However, because the latitudinal temperature gradient is larger in the surface ocean than in the shallow subsurface ocean, SST calibrations have larger TEX_{86}-temperature slopes than SubT calibrations. Consequently, application of TEX_{86}-SST calibrations expectedly leads to an overestimation of SST variability (Ho and Laepple, 2016). Importantly, while absolute SSTs remain challenging to accurately reconstruct, here we prioritize the reconstruction of SST variability. For this, a combined SubT and SST calibration approach gives a proper lower ($SubT_{100\text{-}250}$-calibration) and upper (TEX_{86}^{H}-SST calibration) estimate of SST change. Hence, relative SST changes will be reported here as ΔSubT–ΔSST.

BrGDGTs are membrane lipids that are generally associated with soil bacteria, but are also produced in river, or coastal marine environments (Peterse et al., 2009; Zell et al., 2013; Sinninghe Damsté, 2016). Their abundance relative to that of crenarchaeol, an isoGDGT exclusively produced by marine Nitrososphaerales is generally used to trace terrestrial organic matter input into a marine system, and identify possible terrestrial isoGDGT contribution. For this, we applied the branched and isoprenoid tetraethers (BIT) index (Hopmans et al., 2004) (Equation 2), where samples with higher values (>0.4; Weijers et al., 2006) are customarily associated with dominant contributions of terrestrial organic matter, and left out of the TEX_{86} dataset.

$$BIT\ index = \frac{brGDGT{-}Ia + brGDGT{-}IIa + brGDGT{-}IIa' + brGDGT{-}IIIa + brGDGT{-}IIIa'}{Cren + brGDGT{-}Ia + brGDGT{-}IIa + brGDGT{-}IIa' + brGDGT{-}IIIa + brGDGT{-}IIIa'} \qquad (2)$$

To assess the primary source of brGDGTs, i.e., soil vs marine, we determined the weighted number of cyclopentane moieties in tetramethylated brGDGTs ($\#rings_{tetra}$) (Equation 3), as brGDGTs produced in the marine realm are characterized by a higher degree of cyclisation (Peterse et al., 2009; Sinninghe Damsté, 2016). Furthermore, we calculated the ratio of acyclic hexa- to pentamethylated brGDGTs (IIIa/IIa) (Equation 4), which is positively correlated to marine *in situ* production of brGDGTs (Xiao et al., 2016). Specifically, in the modern system, soils typically show IIIa/IIa ratios below 0.59 and marine sediments show ratios above 0.92 (Xiao et al., 2016, 2020). Additionally, we used the total GDGT assemblage (isoGDGTs + brGDGTs) to infer the depositional setting using the machine learning algorithm "BigMAC" (Martínez-Sosa et al., 2023), capable of distinguishing marine, lake, peat and soil settings.

$$\#rings_{tetra} = \frac{brGDGT{-}Ib + 2 \times brGDGT{-}Ic}{brGDGT{-}Ia + brGDGT{-}Ib + brGDGT{-}Ic} \qquad (3)$$

$$IIIa/IIa = \frac{brGDGT{-}IIIa + brGDGT{-}IIIa'}{brGDGT{-}IIa + brGDGT{-}IIa'} \qquad (4)$$

The degree of methylation of 5-methyl brGDGTs, which in soils correlates to mean annual temperatures (Weijers et al., 2007), was calculated using the Methylation of Branched Tetraethers index (MBT'5me; De Jonge et al., 2014) (Equation 5). For the samples with presumed soil-dominated brGDGT sources (i.e., BIT index > 0.4) we translated MBT'5me index values to mean air temperatures for months above freezing (MAF) using the $BayMBT_0$ calibration (Dearing Crampton-Flood et al., 2020). Roman numerals in all equations refer to molecular structures in De Jonge et al. (2014).

$$MBT'_{5me} = \frac{brGDGTIa + brGDGT{-}Ib + brGDGT{-}Ic}{brGDGT{-}Ia + brGDGT{-}Ib + brGDGT{-}Ic + brGDGT{-}IIa + brGDGT{-}IIb + brGDGT{-}IIc + brGDGT{-}IIIa} \quad (5)$$

2.5 Palynology

Forty-four samples were prepared for palynological analysis, predominantly concentrated between 368.9 and 371 mcd. Between 0.84 and 2.09 gram of sample was crushed to ~0.5 cm chunks and weighed. Next, the sample was transferred to a plastic beaker and one tablet containing a known amount of *Lycopodium clavatum* spores was added. Any carbonates were removed by adding 10% HCl and after settling, the liquid was removed by decantation. Next, silicates were removed by two 40% HF treatments, followed by adding 30% HCl, thereby decanting the liquids after each step and settling/centrifuging. Finally, the sieved residue between 250 and 10 µm was mounted on microscope slides. Total palynomorphs were counted by microscope on 400x to 1000x magnification until at least 100 determinable dinocysts were reached. Count data are combined with previous lower resolution analyses (Sluijs et al., 2009) after a consistency check, reaching a total dataset of 108 samples across Core 27X.

2.6 Spectral analysis

To evaluate the presence and amplitude of orbital frequencies in the our generated records, we performed spectral analysis using Acycle (Li et al., 2019). First, all records were interpolated on 1 cm and subsequently detrended (LOWESS) to remove background trends. Power spectra were generated using the Multi-Taper-Method and tested for significance against 90% and 99% confidence intervals of AR(1) noise. Power was translated to (normalized) amplitude of the signals using a built-in function by Acycle. For bandpass filtering of orbital components, a bandwidth of ~1/5 of the targeted orbital frequency was used. For phase and coherence analysis between two signals, the values were taken at the frequencies that corresponded with the highest coherence within the frequency bands of the targeted orbital components.

3 Results

3.1 Sediment characteristics

Based on the general sediment characteristics and the position of the ETM2 event (Sluijs et al., 2009), we divide the analyzed Core into three sections: the ETM2 event interval (368.0–368.9 mcd), the cyclic pre-ETM2 interval (368.9–371.0 mcd) and the greenish bottom interval (371.0–372.1 mcd) (see Fig. 3).

The MS ranges between 0.4×10^{-8} χ and 2.5×10^{-8} χ, with highest values corresponding to the CIE of ETM2 (Fig. 3d). A gradual decrease in MS values between 372.1–371.0 mcd marks the bottom interval of the core, ending with a high peak at 371 mcd, on the transition from greenish to dark grey sediments. High correspondence between the features in the MS and XRF-based Fe data presented by (Sluijs et al., 2008b) corroborates the general notion that bulk MS variability traces the relative abundance of Fe-rich, magnetic minerals in the sediments. Hence, the decimeter scale variations in Fe content, as previously observed in the pre-ETM2 interval (Sluijs et al., 2008b), are also displayed in the MS record. The cyclic variations within the MS record generally correspond to alternation of dark and light sediment layers with dark layers (low greyscale values) corresponding to high MS and vice versa.

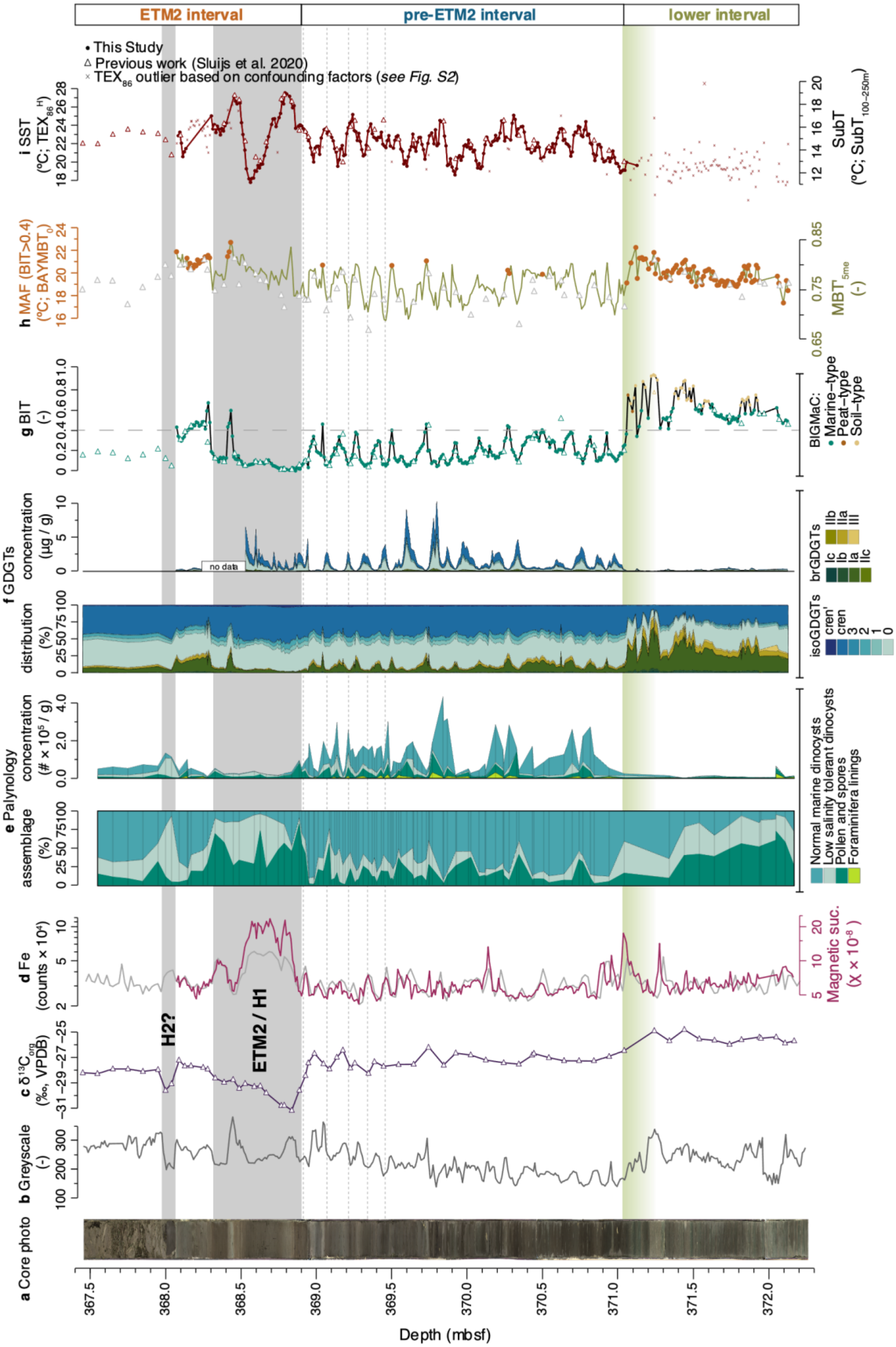
ETM2 interval
pre-ETM2 interval
lower interval
This Study
Previous work (Sluijs et al. 2020)
TEX86 outlier based on confounding factors (see Fig. S2)
i SST
SubT
h MAF (BIT>0.4)
MBT'5me
g BIT
BIGMaC:
Marine-type
Peat-type
Soil-type
f GDGTs
concentration
distribution
no data
brGDGTs
isoGDGTs
e Palynology
concentration
assemblage
Normal marine dinocysts
Low salinity tolerant dinocysts
Pollen and spores
Foraminifera linings
d Fe
Magnetic suc.
c δ13Corg
b Greyscale
a Core photo
H2?
ETM2 / H1
Depth (mbsf)

Figure 3. ACEX Core 27X analysis results. (**a**) Core picture. (**b**) Greyscale. (**c**) Total organic carbon $\delta^{13}C$ (Sluijs et al., 2009). (**d**) MS and Fe (Sluijs et al., 2008b). (**e**) Palynology, with relative abundances of cysts of normal marine, and freshwater tolerant dinoflagellates and pollen and spores, and concentrations of palynomorphs per gram of dry sediment. (**f**) GDGTs, with relative abundances (%) and absolute concentrations (ng/g of dry weight sediment) of all GDGTs. (**g**) BIT index, in which colors of datapoints mark the depositional environment indicated by the BIGMaC machine learning algorithm based on total GDGT distributions (Martínez-Sosa et al., 2023). (**h**) MBT'5_{me} values, where green points mark datapoints with BIT > 0.4, which can be translated to MAF (top axis)). (**i**) TEX_{86}-based SST (bottom axis) and SubT (top axis). Triangles mark data previously generated by (Sluijs et al., 2020), small crosses mark TEX_{86} data influenced by non-thermal factors based on the indices and ratios in Supporting Fig. S2. Grey bars mark hyperthermal events ETM2 and H2, green bar marks a presumed condensed interval.

3.2 Palynological assemblages

Palynomorph assemblages consist predominantly of reasonably to well preserved pollen, spores, and aquatic palynomorphs, typically marine and low-salinity tolerant dinocysts, with locally abundant leiosphaerids (a group of aquatic palynomorphs of unknown affinity). Occasional poor preservation of notably dinocysts causes seven samples too poorly preserved for dinocyst assemblage quantification. The long-term trends, as previously reported by Sluijs et al. (2009), depict high abundances of terrestrial palynomorphs and Peridinioid dinocysts with hexagonal 2a archeopyles – considered to have been produced by low-salinity-tolerant dinoflagellates (e.g., Sluijs and Brinkhuis, 2009; Frieling and Sluijs, 2018) – within the bottom interval and ETM2 (Fig. 3e). The pre-ETM2 interval is marked by considerably lower, but variable concentrations of terrestrial palynomorphs and low-salinity tolerant dinocysts, showing variations of approximately 0–40 % and 5–50 %, respectively, and much higher abundances of species that reflect typical shelf conditions, also consistent with the previous lower resolution work (Sluijs et al., 2009). The concentrations of dinocysts (Fig. 3e) vary between ~1,200 and 550,000 specimens per gram of sediment, with highest concentrations in the pre-ETM2 interval and lowest concentrations in the interval below 371 mcd. Organic linings of benthic foraminifera are present as well, sporadically. Foraminifer linings are mainly concentrated in the pre-ETM2 interval and absent in ETM2 itself.

3.3 GDGTs

3.3.1 GDGT relative abundances and concentrations

Sediments are generally rich in GDGTs with concentrations ranging between 3 and 10,000 ng/g, with highest abundances at 369.755 and 369.555 mcd (Fig. 3f). For 42 samples (368.035–368.505 mcd) GDGT concentrations could not be determined as they were injected without the GTGT standard. At least one of the isoGDGTs was below the detection limit in 13 out of 372 analyzed samples, which were therefore left out of subsequent analyses.

The total GDGT concentrations exhibit clear variability in the pre-ETM2 interval, at the same decimeter-scale as the other records (i.e., greyscale, MS, Fe, terrestrial palynomorphs), with highest total GDGT concentrations in dark, organic and iron-rich layers (Supp. Fig. S1). Total GDGT concentrations are low in the lower interval, with a minimum around 371.0–371. 2

mcd and exhibit low variability. Concentrations of brGDGTs are generally lower than the isoGDGTs, except for a few samples in the lower interval, and range between 0.16–500 ng/g and 0.13–187 ng/g, respectively. Within ETM2, isoGDGTs dominate the total GDGT distributions. The concentrations of brGDGTs closely covary with that of the isoGDGTs in the pre-ETM2 interval. However, the relative proportion of brGDGTs increases during the light-colored intervals (with low total GDGT concentrations) and vice versa.

3.2.2 GDGT distributions

All samples with isoGDGTs above detection limit (n = 359) were screened for potential confounding factors on the TEX_{86} using a set of GDGT ratios and indices established in the literature (Supp. Fig. S2). Specifically, as noticed during the previous low-resolution analyses of Core 27X (Sluijs et al., 2020), the GDGT-2/GDGT-3 ratio is high in the interval leading up to ETM2, reaching up to 13.8, pointing to a clearly dominant GDGT sourcing below the surface mixed layer. Here, we keep all data with GDGT-2/GDGT-3 ratio >5 in the dataset, but interpret it as evidence for isoGDGT contributions from below 200 m (e.g., Hurley et al., 2018). The other isoGDGT indices are predominantly below their defined cut-off values, except for the enigmatic second half of ETM2 (~368 – 368.5), which is marked by high values for the methane index, AOM index, methanogenesis and ΔRI (Supp. Fig. S2), implying that the TEX_{86} - temperature relationship is presumably compromised there because of significant isoGDGT contributions from different archaeal communities.

The $\#rings_{tetra}$ is overall low throughout the complete record (<0.25). Assuming that values >0.7 indicate a marine origin in the modern system (Sinninghe Damsté, 2016), this suggests a dominant terrestrial brGDGT source, consistent with previous ACEX records (Willard et al., 2019; Sluijs et al., 2020). A dominant terrestrial brGDGT sourcing is consistent with the IIIa/IIa ratios, which average 0.51, 0.53 and 0.32 for the ETM2, pre ETM2 and lower intervals, respectively (Supp. Fig. S3).

The BIT index is generally highest in the lower interval (mean = 0.61) and above 368.26 mcd (mean = 0.43), while lowest values are within ETM2 (mean = 0.12). In the pre-ETM2 interval the BIT index regularly varies between 0.06 and 0.51 on decimeter scale (mean = 0.21). Particularly in the lower interval, BIT index values are above the general cut-off of 0.4 that is used to identify a pronounced impact of soil-derived isoGDGTs on TEX_{86} paleothermometry (n = 122) (Fig. 3g, Supp. Fig. S2).

The BIGMaC algorithm indicates a dominant marine depositional environment based on the distribution of the total GDGT pool in the studied interval (Fig. 3g), including 84 samples where more terrestrial input is expected based on higher (>0.4) BIT index values. Samples that BIGMaC classifies as dominantly terrestrial (either peat- or soil-sourced) exclusively occur in the lower interval, characterized by BIT > 0.58 and $\#rings_{tetra}$ < 0.16.

3.3.3 Temperature reconstructions

We translate the isoGDGT distributions into SubTs of ~11–19 ºC following the $SubT_{100-250m}$ calibration. This corresponds to SSTs of ~18–27 ºC using the TEX_{86}^{H} calibration (Kim et al., 2010) (Fig. 3i). Peak temperatures are reached during the ETM2 event, marked by a warming from background SubTs of 13–16 ºC (SSTs = 20–24 ºC) to peak temperatures of 19 ºC (SST = 27 ºC), signifying an averaged warming of 4.5–5.5 ºC (ΔSubT–ΔSST). Apart from the two apparent maxima in the TEX_{86} record related to ETM2 (368.4 and 368.75 mcd), we identify four earlier local SST maxima that occur in intervals of approximately 50 cm: at ~369.25, 369.75, 370.25 and 370.75, with peak SubTs of ~17 ºC (SSTs= ~24–25 ºC). In the pre-ETM2 interval, the SST record also exhibits smaller, decimeter scale cyclic variations, depicting a total variability up to 3–5 ºC (ΔSubT–ΔSST).

The analytical error in the TEX_{86}, determined by the standard deviation of 62 measurements of the in-house GDGT standard, is 0.005 TEX_{86} units. In the TEX_{86} range of the early Eocene Arctic, this analytical error amounts to 0.20 ºC for SubTs and 0.26 ºC for SSTs. Although this uncertainty does not include any potential errors associated with extraction and fractionation, the low analytical error implies high confidence on the reconstructed direction and magnitude of SST variability, which is the prime goal for this study.

Decimeter-scale variations within the MBT'_{5me} record display a high correspondence with the BIT index, where low BIT index values correspond with the lower MBT'_{5me} values and *vice versa*. For the samples with BIT > 0.4 (n = 122), we converted MBT'_{5me} to MAF, resulting in mean temperatures of 20 ºC, and a warming of ~2 ºC to peak temperatures of ~23 ºC associated with the ETM2 (Fig. 3h). A second MAF peak is recorded at ~371.2 mbsf, reaching ~22 ºC. In comparison with the previously published low-resolution data generated on the same instrument in 2018, the BIT values are well in agreement (Sluijs et al. (2020), whereas the MBT'_{5me} values are overall slightly (~0.02) higher (Willard et al., 2019).

4 Spectral analysis and tuning

4.1 Spectral analysis of pre-ETM2 interval

The suite of environmental proxy data (Fig. 3) shows a concentration of apparently cyclic variability in the pre-ETM2 interval of 368.9–371.0 mcd, comprising the most distal marine sequence according to our data, characterized by generally low relative proportions of terrestrial palynomorphs, low BIT index values, and low MS values. Therefore, to analyze the imprint of orbital cycles on Arctic (hydro)climate variability, we focus on the pre-ETM2 interval for spectral analysis, thereby excluding ETM2 itself and the lower interval.

The MTM power spectra (Fig. 4a) show that the observed regular decimeter-scale variability in the generated records in the pre-ETM2 interval are expressed as significant spectral components for nearly all datasets generated in this study. The analyzed datasets exhibit dominant frequencies of 1.5–2.5 cycles / m (mainly TEX_{86}, but also MS; pollen/spores), 4–6 cycles / m (GDGT concentrations; BIT index; MBT'_{5me} index; TEX_{86}; pollen and spores) and 8–10 cycles / m (BIT index; MBT'_{5me} index; greyscale), representative of periodicities of approximately 50, 22 and 10–14 cm, respectively. The ratio between the predominant 50, 22, 10–14 cm periodicities approximates the ratio between ~100-kyr eccentricity, 41-kyr obliquity and 22-kyr precession. This hypothesis is substantiated by a close relation between the amplitude modulation of the 10–14 cm precession related cycles (e.g., in greyscale and total GDGT concentration) by ~50 cm eccentricity cycles (i.e., in TEX_{86}) (**Fig. 5**). Spectral analysis of the XRF-based Fe record across a much larger interval (Cores 29X–27X; Sluijs et al., 2008b), found slightly lower frequencies, but consistent ratios indicating the same orbital forcing. Consequently, following above cyclostratigraphic interpretation, sedimentation rate in the here-studied interval was ~0.5 cm / kyr, which compares well to the 0.6–0.7 cm / kyr based on chemostratigraphic constraints for the larger interval (Sluijs et al. 2008). The slight offset could relate to a reduced siliciclastic sediment input during this interval, because the pre-ETM2 interval covers the most distally marine depositional setting of the analyzed sections by Sluijs et al. (2008).

We tune our record to the astronomical solution based on the solid, orbitally tuned, age constraint of the ETM2 event starting at 54.005 Ma, and the clear expression of the ~100-kyr eccentricity cycles in the TEX_{86} record, of which the phase relation is deduced from its amplitude modulation of precession in several other records (**Fig. 5**). We identify four 100-kyr eccentricity maxima, which we tune to the maxima of 54.15, 54.25, 54.35 and 54.45 Ma of the La10b eccentricity solution (Laskar et al., 2011).

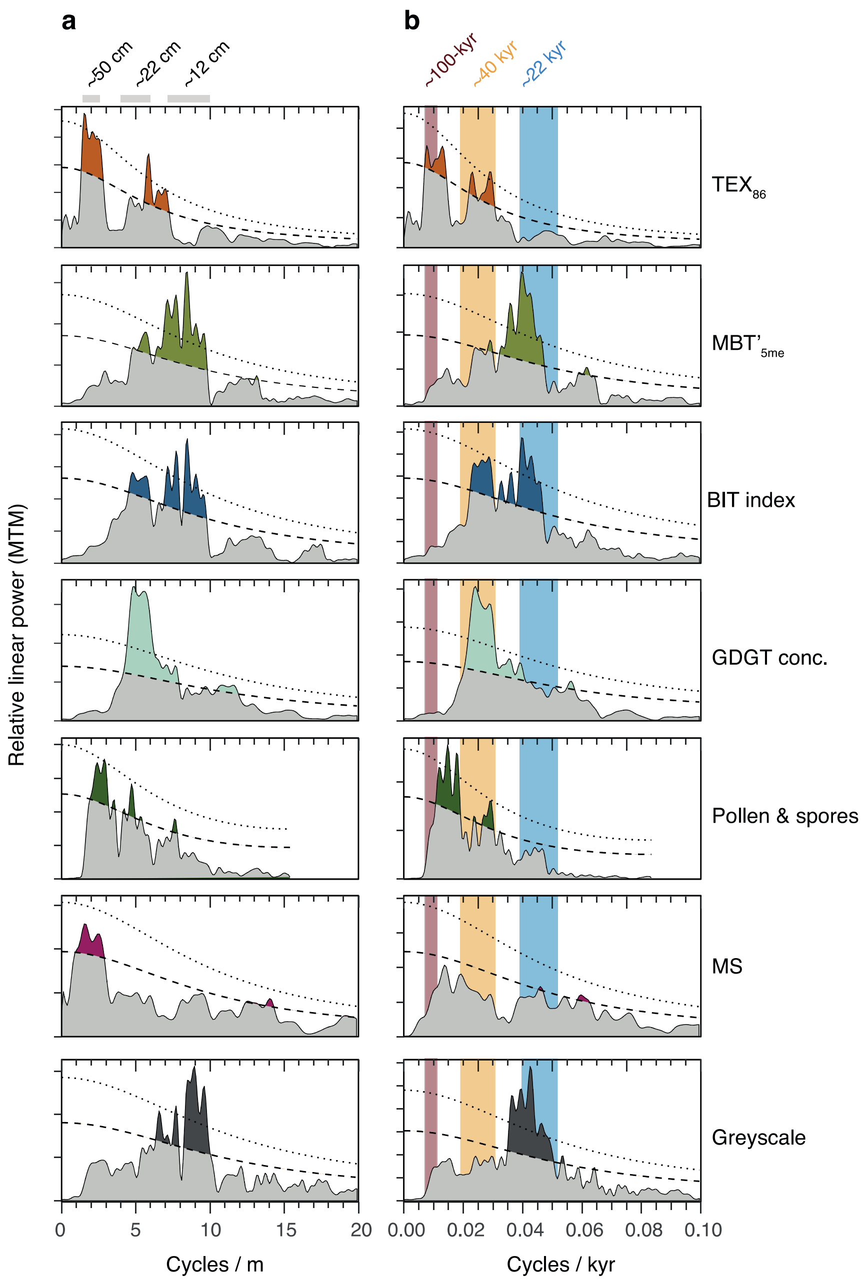

Figure 4. MTM Power spectra in depth (**a**) and age (**b**) domains. Dashed and dotted lines indicate 90% and 99% confidence intervals of AR(1), respectively.

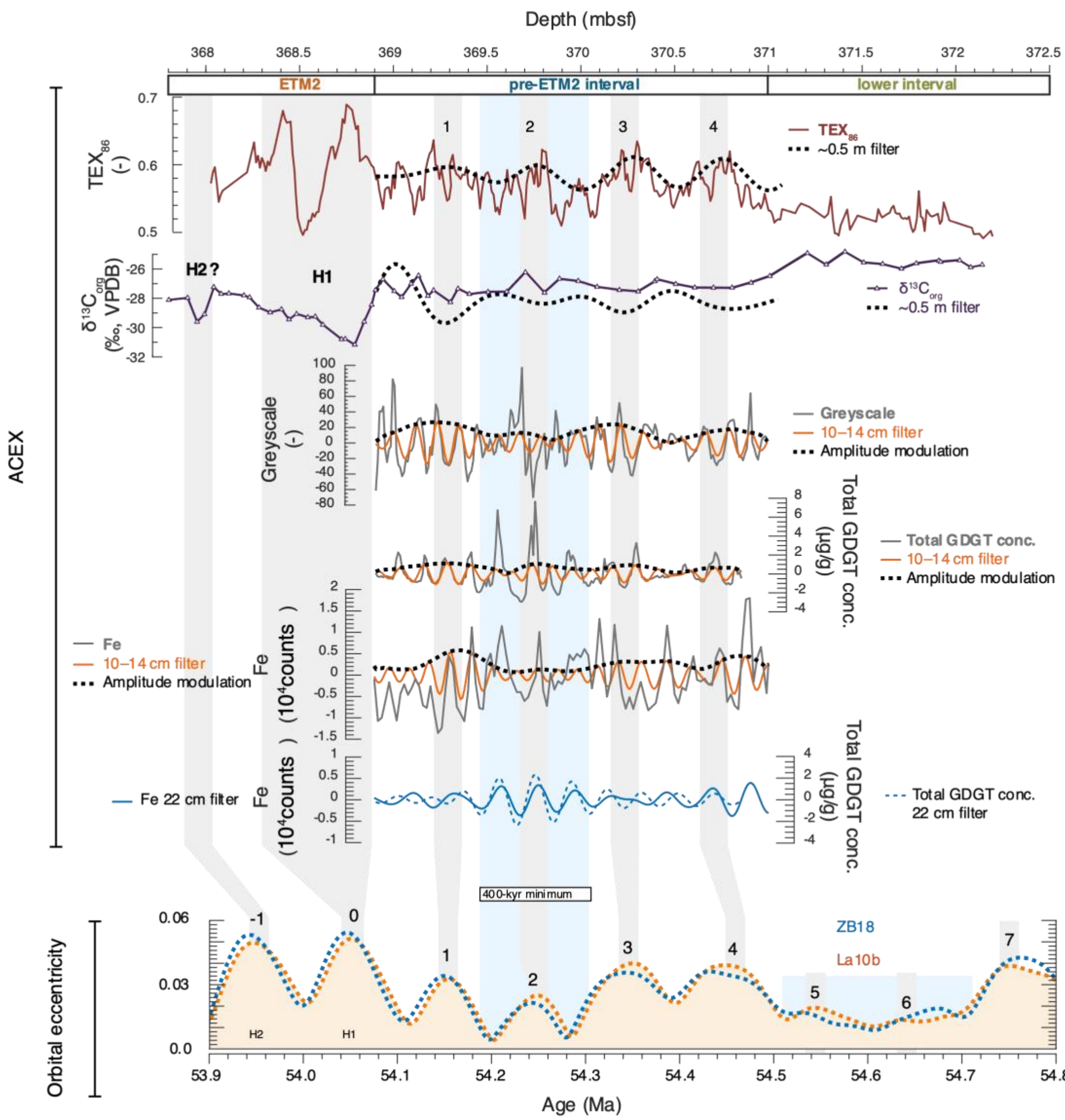

Figure 5. Tuning of the pre-ETM2 interval of ACEX to eccentricity. Eccentricity maxima are numbered relative to the ETM2 related maximum.

After tuning, spectral analysis in the age domain (Fig. 4b) indicates that BIT, MBT'_{5me}, greyscale and MS exhibit dominant periodicities in the precession band, whereas TEX_{86} and total GDGT concentrations exhibit dominant obliquity frequencies. Records of terrestrial palynomorphs have less clearly pronounced forcing by the identified astronomical cycles, likely due to the lower sample resolution than the other proxy records, but a modest signal of obliquity is present. The imprint of short eccentricity is most clearly expressed in the power spectrum of

TEX_{86}. Interestingly, a dominant ~17 cm periodicity of the TEX_{86} record amounts to ~33 kyr following our tuning. Indeed, obliquity has a ~30 kyr component (Fig. 2) derived from the secular resonance of $p + s2$. However, this is only a minor component compared to the dominant obliquity of ~41 kyr. A significant periodicity of ~30 kyr in Pleistocene records is typically ascribed to a combination tone (e.g., Lourens et al., 2010), such as short eccentricity and obliquity (1/100 + 1/41 = 1/29), double obliquity and single obliquity (1/82 + 1/41 = 1/27) or 19-kyr precession and obliquity (1/19 - 1/41 = 1/35). As this frequency is only dominantly present in the TEX_{86} record, which shows significant forcing by short eccentricity and obliquity, we presume that this ~30 kyr cycle is a combination tone of the 100-kyr eccentricity and 41-kyr obliquity cycles.

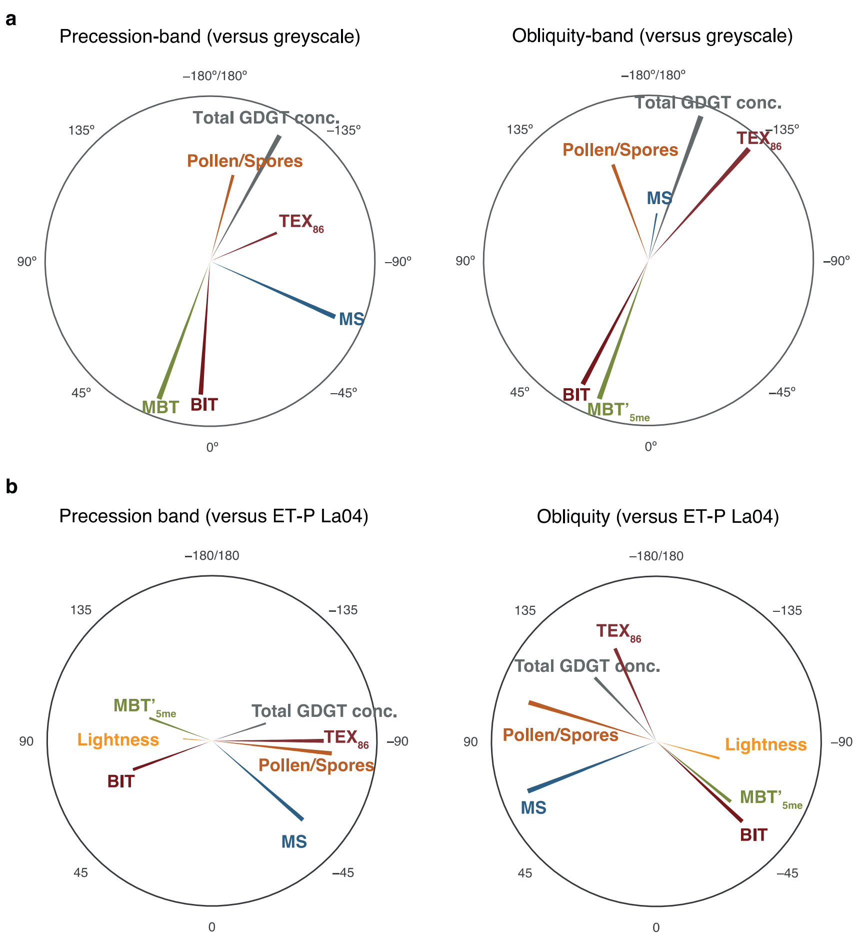

Figure 6. Phasing of proxy records in precession and obliquity bands. Phases are plotted as degree difference to the sediment greyscale record (**a**) and to ETP (negative precession) of La04 (**b**). Length of the bars indicate correspondence.

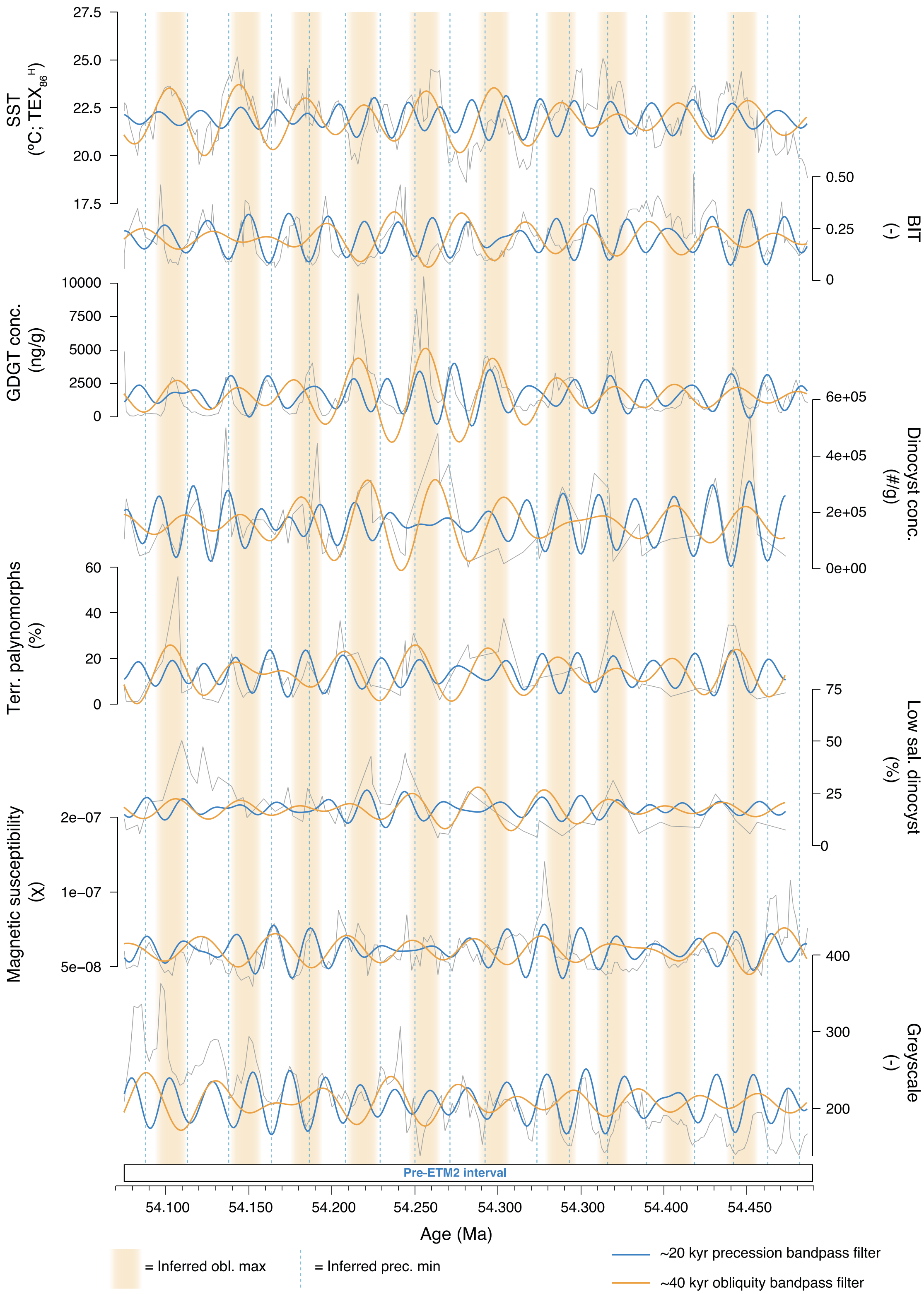

Figure 7. Tuned paleoenvironmental proxy data across the pre-ETM2 interval of ACEX and bandpass filters for precession (**a**) and obliquity (**b**). Orange bars mark inferred obliquity maxima; blue dotted lines mark inferred precession minima.

4.2 Amplitude and phasing

The correspondence and phasing of the precession and obliquity signals were calculated relative to the sediment color and to the orbital solution (Fig. 6). Note that the precession and obliquity components of the orbital solution are subject to uncertainty in the early Eocene, due to chaotic behavior in the solar system (Laskar et al., 2004; Zeebe and Lourens, 2019), and their respective phasing is not considered in absolute sense. Nevertheless, they provide a steady and independent rhythm for comparison between the other proxy-derived components. On both precession and obliquity timescales there is a correspondence between the BIT index, MBT'_{5me} index, and greyscale, in antiphase with TEX_{86}, total GDGT concentrations, and terrestrial palynomorphs (Figs. 6, 7). MS is approximately in phase with the TEX_{86}, terrestrial palynomorph abundances, and total GDGT concentrations, but shows a conspicuous general lead (or lag) with respect to the other records. Remarkably, temperature proxies TEX_{86} and the MBT'_{5me} index are in near antiphase across the orbitally driven variations in the pre-ETM2 interval. Similarly, terrestrial palynomorph abundances and the BIT index, both indicators for terrestrial input, are in antiphase for most of the record.

For multiple records (including Fe and total GDGT conc. (Figs. 5, 7), highest imprint of obliquity cycles (and reduced imprint of precession) is concentrated between 54.180 and 54.320 Ma, coinciding with a 400-kyr eccentricity minimum. The correspondence between long-term eccentricity nodes and the emergence of obliquity in paleoclimate signals has been observed for other intervals and locations (e.g., Westerhold et al., 2014).

5 Discussion

5.1 Relative sea level change

The sediments of the lower interval (<371 mcd) are likely deposited in a proximal marine setting, just below wave base. This is evidenced by the high BIT index values, peat/soil-derived GDGT distributions assigned by the BigMAC algorithm, high proportions of terrestrial palynomorphs, high proportions of low-salinity-dominant dinocysts, low abundance of normal marine dinocysts, and low GDGT-2/GDGT-3 ratios. Contrastingly, the pre-ETM2 interval is characterized by a more offshore marine depositional setting, evidenced by low BIT index values, marine-associated GDGT distributions, low proportions of terrestrial palynomorphs, high GDGT-2/GDGT-3 ratios, and dominance of normal marine dinocysts. Specifically, one critical observation for a deeper environmental setting in the pre-ETM2 interval are the high GDGT-2/GDGT-3 values in the preETM2 interval (mean = 7.8 (SD=2.2); Supp. Fig. S2). In the modern, marine sedimentary GDGT-2/GDGT-3 ratios below 5 indicate an isoGDGT export depth from maximally 150 – 200 m water depth, but ratio values rapidly increase with GDGT contributions from deeper waters because of contributions of a distinct deeper dwelling Nitrososphaerales clade (Taylor et al., 2013; Hurley et al., 2018; van der Weijst et al., 2022; Rattanasriampaipong et al., 2022). Crucially, GDGT assemblages with GDGT-2/GDGT-3 ratios exceeding 5 are rarely produced shallower than 200 m depth (Taylor et al., 2013; Hurley et al., 2018). While we acknowledge that the non-analogue situation of the Eocene Arctic might have led to anomalous GDGT ratios, GDGT-2/GDGT-3 ratios averaging 7.8 strongly suggest that the paleodepth reached deeper than 200 m during the pre-ETM2 interval.

The boundary between the lower and pre-ETM2 interval (~371.0 – 371.2 mcd; dated at ~54.55 Ma) is characterized by an organic-lean interval of numerous multi-cm-scale green layers, presumably rich in glauconite (Sluijs et al., 2020). We surmise that this interval marks a condensed section that spans the onset of a transgression, when increasing landward accommodation space reduces the sedimentation on the distal shelf. The magnitude of relative sea level change across this interval was presumably at least 100 m, if the lower interval was deposited close to wave base and the pre-ETM2 interval was deposited at water depths exceeding 200 m. Therefore, this sea level rise was likely initiated by a phase of (cooling induced) subsidence of the Lomonosov Ridge around 54.55 Ma, following its Paleocene rifting. Given some evidence of potentially coeval transgressive surfaces in the North Sea (Powell et al., 1996) and New Jersey (sequence E1 of Browning et al. (1996)), some effect of eustacy cannot be excluded (Sluijs et al., 2008a). However, given the absence of large ice sheets during this time interval, the relative contribution of eustatic rise would be negligible considering the large magnitude of sea level rise recorded at Lomonosov Ridge. The return to dominant low-salinity-tolerant dinocysts in younger strata above Core 27X — for which the exact depth and age is poorly constrained due to the lack of sediment recovery between the top of Core 27X at 367.4 mcd and the bottom of Core 23X at ~345 mcd, but presumably in the Early Eocene Climatic Optimum (Sluijs et al., 2008b) — suggests that Lomonosov Ridge was uplifted again to resume very proximal marine sedimentation at the drill site.

5.2 Orbitally forced GDGT sourcing in the pre-ETM2 interval

5.2.1 Terrestrially versus marine-sourced brGDGTs

Curiously, in the relatively distal and deep marine pre-ETM2 interval, variations in BIT index values negatively correlate to brGDGT concentrations and terrestrial palynomorph abundances on precession and obliquity timescales (**Figs 3, 6, 7**). Minima in the BIT index counterintuitively coincide with maxima in brGDGT concentrations, but also even higher maxima in concentrations of marine isoGDGT crenarchaeol. Given that the orbital age model excludes changes in siliciclastic sediment supply sufficient to dilute and concentrate GDGTs across orbital cycles, this strongly suggests that marine productivity of isoGDGTs during these periods outcompeted the additional terrestrial supply of brGDGTs, hence lowering the BIT index. We infer that the most likely mechanism behind this phasing is that periodically enhanced terrestrial nutrient supply due to hydrological and temperature change triggered marine productivity of both isoGDGTs and brGDGTs on the shelf. Indeed, elevated marine productivity coinciding with intervals of peak GDGTs is supported by the overall higher organic content in these (predominantly darker; **Fig. 3**) sediment layers, albeit based on few TOC% measurements by Sluijs et al. (2008b) (**Supp. Fig. S1)**.

A significant contribution of in-situ marine produced brGDGTs is on first sight contrasted by overall low $\#rings_{tetra}$ values throughout the record (<0.25), i.e., values generally associated with a primarily soil-derived brGDGT origin. However, the negative correlation with the BIT index, reminiscent of modern shelf transects (Sinninghe Damsté, 2016) (**Supp. Fig. S4**), suggests a degree of covariance between shifts in terrestrial versus marine brGDGT sourcing and the BIT index. This relationship is further evidenced by the negative relationship between the BIT index and the brGDGT IIIa/IIa ratio (**Supp. Fig. S3**). Collectively, particularly considering the antiphase behavior of BIT index values and terrestrial palynomorph abundances, we interpret that in the pre-ETM2 interval, the BIT index specifically traces the relative contribution of soil-derived brGDGTs to the total brGDGT pool, while the terrestrial palynomorph abundances track the absolute terrestrial input.

5.2.2 Shallow versus deep sourced isoGDGTs

Exclusively temperature-controlled distributions of isoGDGTs would result in a negative relation between TEX_{86} and GDGT-2/GDGT-3 ratios, simply because Nitrososphaerales increase the number of cyclopentane rings with increasing temperature to maintain membrane rigidity (e.g., Schouten et al., 2002; Rattanasriampaipong et al., 2022). However, similar to the modern ocean surface sediments (Taylor et al., 2013; Rattanasriampaipong et al., 2022) and many downcore records (e.g.,van der Weijst et al., 2022), the GDGT2/GDGT3 ratio weakly positively correlates with TEX_{86} in the studied section ($R^2 = 0.25$; Supp. Fig. S5a). In the modern system, this feature has been linked to increased contribution by deeper-dwelling (below pycnocline) GDGT-producers (Rattanasriampaipong et al., 2022). Within the pre-ETM2 interval, the fluctuations of the GDGT-2/GDGT-3 ratio strongly covary with the obliquity and precession scale variations recorded in TEX_{86}. This suggests varying proportional contributions of deeper and shallow living GDGT-producers on orbital timescales.

In the absence of significant early Eocene ice sheets, it is unlikely that orbitally forced relative sea level variability was responsible for the observed fluctuations in GDGT-2/GDGT-3. Therefore, we postulate the recorded GDGT-2/GDGT-3 fluctuations to reflect orbitally forced changes in water column structure, for instance through vertical movement of the nitracline depth, periodically allowing for increased GDGT contributions of a deeper dwelling community. The strong negative correlation between GDGT-2/GDGT-3 and BIT index ($R^2 = 0.51$; Supp. Fig. S5b) suggests that these water column fluctuations are coeval with marine productivity changes (*see 5.2.1*).

Importantly, such contributions of deeper dwelling communities do not necessarily impair the TEX_{86}-temperature relationship, as there is no primary control of GDGT-2/GDGT-3 ratios on the TEX_{86} (see Equation 1). Suspended particulate matter from >200 m water depth typically has GDGT-2/GDGT-3 ratios >20 (Hurley et al., 2018), and this likely includes GDGTs exported from shallow waters, suggesting that deep dwelling communities produce GDGTs in much higher GDGT-2/GDGT-3 ratios. Average GDGT-2/GDGT-3 ratios of 7.8 therefore only indicate relatively modest GDGT contributions from deeper waters. This is further supported by reconstructions from the Chilean and Angolan margins, where sets of neighboring sites with substantially different water depths and GDGT-2/GDGT-3 ratios, yield very comparable TEX_{86} records (Varma et al., 2023).

5.3 Orbital climate variability of the early Eocene Arctic

5.3.1 Temperature

Our spectral analyses support the notion that the decimeter-scale variability across the ACEX pre-ETM2 record, as captured in the TEX_{86} record, is associated with orbital cyclicity (**Figs. 4, 7**). The orbital-scale variation of SST has a strong imprint of obliquity and eccentricity (**Fig. 4**), with the TEX_{86} MTM spectrum indicating amplitudes of 0.5–0.7 ºC and 0.7–0.8 ºC, respectively (**Supp. Fig. S6**). Variability in the precession band, visible as a small peak in the MTM spectrum of TEX_{86}, but below 0.9 AR(1), only has a limited amplitude of ~0.2–0.3 ºC. Note that the analytical uncertainty has minimal effect on the reconstructed spectral amplitudes, as this error is normally distributed around the targeted signals. Crucially, the completeness of the cyclicity of the reconstructed SST signal indicates that the complete orbital imprint of SST was reconstructed, demonstrating that there is no bias to one end of the orbital cycle in the sedimentary record of the early Eocene Lomonosov Ridge.

In lack of independent data on orbital phasing of the precession and obliquity signals and other driving mechanisms (e.g., the role of atmospheric heat transport), we interpret the SST maxima as insolation maxima at 78ºN. Without a-priori knowledge on seasonality of forcing, insolation maxima at a latitude of 78ºN correspond to obliquity maxima (Fig. 9), and, if biased towards summer, to precession minima (Fig. 2).

The MBT'_{5me} record displays a clear influence of orbital cyclicity as well (Fig. 4). The antiphase of the orbital signals between MBT'_{5me} and TEX_{86} in the pre-ETM2 interval (Fig. 6) corroborates the inferred changes in terrestrial vs marine-sourced brGDGTs (*see 5.2.1*), because it is virtually impossible that continental air temperature varies oppositely of near-shore SSTs. Therefore, we interpret the orbital variation captured in the MBT'_{5me} record to signify variability in brGDGT sourcing, rather than MAF variability. Interestingly, the MAF reconstructed from samples with BIT > 0.4, which we deem to contain mostly soil-dominated brGDGTs, is approximately ~20–21 °C in the pre-ETM2 interval (calibration error = 3.8 ºC (Dearing Crampton-Flood et al., 2020)), and approximately compatible with the minima in TEX_{86}^{H}-based SSTs (**Fig. 3**), and pollen derived estimates form this interval (Willard et al., 2019). Furthermore, based on these samples, we reconstruct a MAF increase during the peak ETM2 interval of ~2 ºC, reaching a maximum of 22.7 ºC at 368.3 mcd.

5.3.2 Hydrology and marine productivity

Cyclic variability in the supply of terrestrial palynomorphs to the Arctic Basin suggests an orbital control on Arctic hydrology in the early Eocene, fitting records of the middle Eocene (Sangiorgi et al., 2008; Barke et al., 2011). Furthermore, indicators for marine productivity (i.e., total GDGT concentration, TOC content, in the absence of strong changes in sediment accumulation rates) all peak during maxima of terrestrial palynomorphs, suggesting a strong increase in terrestrial nutrient supply to the basin on orbital timescales, presumably through increased runoff (*see 5.2.1*). This signal is in line with the cyclic shift in brGDGT sourcing from marine in-situ dominated (i.e., low BIT) during the phases of high runoff, and terrestrially dominated (i.e., high BIT) during the phases of low runoff.

The orbital imprint on early Eocene Arctic temperature and hydrology was likely forced by a combination of variable regional moisture circulation and variable poleward (heat and) moisture transport. Interestingly, the phasing of these two processes is opposite on obliquity timescales: obliquity maxima result in maximum high-latitude summer insolation, and consequently higher evaporation/precipitation rates, whereas obliquity minima result in an enhanced meridional insolation gradient on the summer hemisphere (e.g., Raymo and Nisancioglu, 2003), and consequently an intensified poleward moisture transport (Loutre et al., 2004). If poleward moisture transport was the dominant process causing the hydrological variability, precipitation maxima would occur during obliquity minima. In contrast, we find an in-phase relationship between runoff indicators and TEX_{86} on both obliquity and precession timescales (**Figs. 6, 7**), which implies that the runoff was in-phase with temperature, and presumably also with insolation.

While we acknowledge the lack of independent constraints on the phase relation between our records and astronomical cycles, the positive temperature-runoff phasing strongly suggests that the orbital variation of poleward moisture transport originating from the (sub)tropics was subordinate to that of the regional, high-latitude, hydrological processes. Collectively, this implies that orbitally forced insolation maxima (e.g., obliquity maxima and/or precession minima modulated by eccentricity) caused warmer and more humid conditions in the Arctic region, and this was expressed by increased regional evaporation, precipitation, erosion, and runoff, and increased primary and secondary production in the coastal realm.

A poleward expansion of convective precipitation due to the diminished early Eocene meridional temperature gradient (Speelman et al., 2010) might have led to a more proximal forcing of high-latitude moisture supply. It is plausible that the humidity was sustained by deep convection happening in the high latitudes, as suggested by certain model simulations of ice-free polar conditions (Abbot and Tziperman, 2008a, 2008b), and presumably strongly influenced by summer insolation, possibly even resulting in a monsoon-like climate at high latitudes (Baatsen et al., 2024). Interestingly, such high latitude deep convection might present an important feedback mechanism for extratropical amplification of climate variability, and maintaining above-freezing winter temperatures (Abbot and Tziperman, 2008a). This mechanism starkly contrasts the Pleistocene situation, when obliquity modulated the moisture transport from lower latitudes through insolation gradients (Vimeux et al., 2001; Masson-Delmotte et al., 2005), while polar temperatures predominantly varied in-phase with insolation (Kindler et al., 2014; Uemura et al., 2018). Hence, it can be argued that the effects of (sea) ice cover, high albedo and much colder high-latitude SSTs in the Pleistocene greatly minimized the effects of high-latitude summer insolation maxima on hydrological processes, while they were dominant in the early Eocene.

As noted in previous work, the PETM and ETM2 events in the early Eocene Arctic were paired with massive hydrological changes (Sluijs et al., 2006, 2009; Pagani et al., 2006; Krishnan et al., 2014), here corroborated by our higher resolution biomarker and palynology data. Interestingly, our orbital age model now allows for determining sedimentation rate changes. Based on our determined background sedimentation rates of 0.5 cm/kyr and the 56 cm interval covering the peak ETM2 CIE and recovery at Lomonosov Ridge, which corresponds to a ~60 kyr time interval (Stap et al., 2010), we infer a factor 1.8 sedimentation rate increase to ~0.9 cm/kyr. While this accumulation rate increase is smaller than the recorded three- to fivefold increase during the PETM (Sluijs et al., 2008b), together with the enhanced iron accumulation it confirms the increased terrestrial sediment supply during the event, likely due to an intensified hydrological cycle.

5.4 Seasonality of the proxy records

Variations in Earth's axial precession have multiple implications for the insolation that reaches Earth. The first order control is the proximity to the sun, as precession determines the season that coincides with peri/aphelion. However, due to conservation of angular momentum, Earth moves faster when it is closer to the sun and the season at perihelion is therefore also the shortest season (Loutre et al., 2004). Consequently, if insolation is averaged across the complete summer, this effect almost entirely counters the positive effect of perihelion during summer solstice (Huybers, 2006). Obliquity, on the other hand, has a more straight-forward effect on regional insolation, especially in the polar regions, where its direct effect is restricted to mainly influencing summer radiation. Together, due to their different mechanisms, the relative imprint of obliquity and precession on a climatic parameter depends on the duration and season of forcing (see **Fig. 2**).

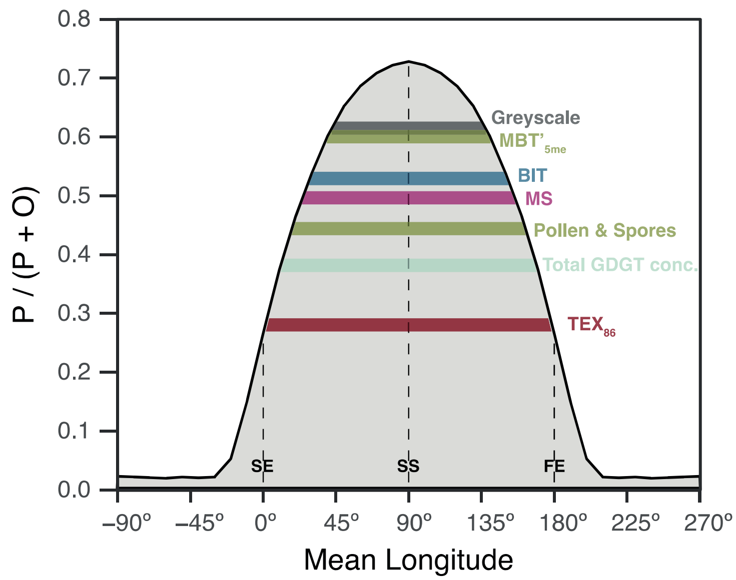

Figure 8. Precession/obliquity index of insolation for different periods surrounding the summer solstice. Positions of the spring equinox, summer solstice and fall equinox are marked by dashed lines. Plot based on MTM spectra of La04 insolation curve (Laskar et al., 2004) at 78°N during the pre-ETM2 interval. SE = spring equinox, SS = summer solstice, FE = fall equinox.

When we assume a direct coupling between local insolation and proxy response, and a forcing centered around the summer solstice, the precession and obliquity index distribution at 78°N (precession / (precession + obliquity; P / (P + O)) has a bell-shaped pattern (Fig. 8). Similar index values, calculated from spectral amplitudes from our proxy records, show that our orbital proxy variability is forced by different orbital components, some that show strong imprint of precession (e.g., greyscale and MBT'_{5me}), and some with much stronger obliquity (TEX_{86} and total GDGT concentration). Crucially, the TEX_{86} spectrum dominantly shows obliquity and very low (or absent) precession (P / (P + O) = 0.28), which takes it very far from a short (peak) summer forcing. Rather, a forcing from start of spring to start of fall is more in line with the orbital imprint. Note that, as the precession component of the TEX_{86} frequency spectrum is below the 0.9 CI of AR(1) noise (Fig. 4), the forcing period is essentially indistinguishable from annual averaged forcing (Fig. 8). However, the clear expression of multiple precession cycles in the filtered TEX_{86} record during certain eccentricity maxima (e.g., at 54.350 and 54.250, Fig. 7) suggest that a small component of precession is indeed present, and corroborates the spring–fall forcing of this signal.

The other signals (i.e., greyscale, MBT'_{5me}, BIT, MS, Pollen & Spores, GDGT concentration) associated with hydrological variability on land and associated marine productivity have higher relative influence of precession. The signals with higher influence of precession implies that either the period of forcing was a shorter period around the solstice, or that it was more skewed towards one season. The dominant imprint of precession on the hydrological indicators at the Lomonosov Ridge could therefore resemble a mechanism that is reminiscent of precession influenced low-latitude monsoonal systems, where summer insolation maxima dominate monsoon intensity (Kutzbach and Otto-Bliesner, 1982; Kutzbach et al., 2008). A strong seasonal precipitation in the early Eocene Arctic, as our orbital interpretation suggests, has been supported by strong seasonal $\delta^{13}C$ variations in fossilized wood (Schubert et al., 2012), but is contrasted by fossil leaf and pollen analyses (West et al., 2015; Willard et al., 2019).

5.5 Arctic endmember of eccentricity-forced global temperature variability

The imprint of 100-kyr orbital eccentricity on pre-ETM2 SSTs at the Lomonosov Ridge margin, while the direct influence of eccentricity on insolation is minor, confirms previous studies of the early Eocene that find high imprint of this cycle on temperature variability (e.g., Lauretano et al., 2018; Fokkema et al., 2023), even if the major imprint of eccentricity on the occurrence of hyperthermals is ignored. We analyze the imprint of the short-eccentricity cycle on temperature during the pre-ETM2 interval by comparing the signal of ACEX to that reconstructed by benthic foraminiferal carbonate oxygen isotope ratios from Walvis Ridge ODP Site 1262 (Stap et al., 2010; Littler et al., 2014). While the resolution of the benthic isotope records is suboptimal in the pre-ETM2 interval, we find an amplitude of eccentricity variability of ~0.3 ºC (Fig. 9; Supp. Fig. S6), which is 2 – 3 times smaller than our recorded variability (~0.7–0.8 ºC) at the Lomonosov Ridge. While both records reflect high latitude signals, the higher latitude of the ACEX (78º N) compared to the bottom-water formation areas in the Southern Ocean (~60-65 °S; Lunt et al., 2021) could lead to an amplified signal at ACEX, however the magnitude of amplification remains high.

In lack of contemporary tropical SST records, we additionally compare to a record from the tropical Atlantic that just succeeds the studied pre-ETM2 interval (53.7–52.0 Ma) from the Eastern Equatorial Atlantic (Fokkema et al., 2023) (Site 959; paleolatitude = ~9ºS). At Ocean Drilling Program (ODP) Site 959, the amplitude of SST variability associated with short-eccentricity outside the hyperthermals is approximately 0.2–0.3 ºC. The significantly higher variability that we reported compared to the tropics suggests that the temperature variations associated with short-term eccentricity were amplified by a factor of 3–4 at Lomonosov Ridge margin compared to the tropical Atlantic Ocean.

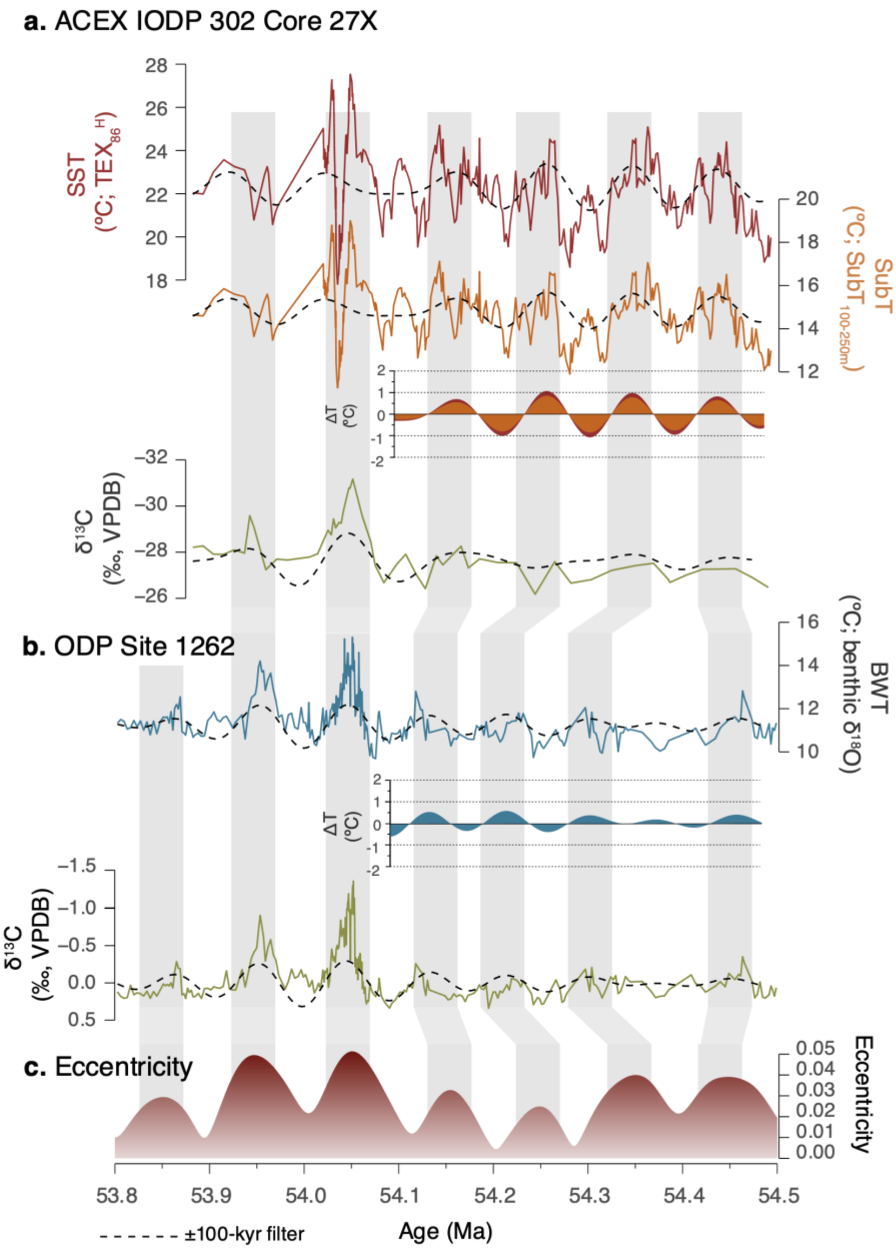

Figure 9. Comparison of eccentricity-scale temperature variability between this study and the open ocean benthic record of ODP Site 1262. **(a)** ACEX SST/SubT with 100-kyr eccentricity filters, and organic $\delta^{13}C$ record. (**b**) Open ocean bottom water temperatures (BWTs) and $\delta^{13}C$ from ODP 1262, with 100-kyr eccentricity filters. BWTs are based on benthic foraminiferal $\delta^{18}O$. (**c**) Orbital eccentricity (Laskar et al., 2011). For ODP Site 1262, minor deviations of the age model by Westerhold et al., (2017) were made to line up the $\delta^{13}C$ and $\delta^{18}O$ minima with the eccentricity maxima. The amplitude of SST variability from the ACEX is presented as a range, using both an SST (TEX_{86}^{H}) and SubT ($SubT_{100\text{-}250m}$) calibration.

6. Conclusions

The high-resolution organic biomarker, palynological and geochemical analyses presented in this work allow for the reconstruction of complete Milankovitch climate variability at the early Eocene Lomonosov Ridge. Insolation variability invoked by obliquity and precession cyclicity caused temperature variations up to 1.0–1.4 and 0.4–0.6 ºC, respectively. Utilizing the relative spectral amplitudes of the precession and obliquity frequencies in the TEX_{86} record, we infer that the reconstructed temperature variability represents a spring-to-fall forced signal.

The TEX_{86} maxima correlate to maxima in terrestrial organic supply to the Arctic basin, notably evidenced by peak abundances in terrestrial palynomorphs, suggesting that regional insolation maxima (precession minima / obliquity maxima) dominated hydrological processes in the Arctic region, causing enhanced precipitation, continental runoff and nutrient input into the basin, and triggering highly productive conditions at the central Lomonosov Ridge. The in-phase relationship on obliquity timescales suggests that regional moisture circulation was the dominant forcing agent on the orbital hydrological response, in contrast to meridional moisture transport which dominated precipitation on orbital timescales in the Pleistocene.

Temperature variations paced by Earth's orbital eccentricity maxima greatly impacted Arctic temperatures as well. Next to the globally defined ETM2 event, where Lomonosov Ridge experienced ~5 ºC warming, 100-kyr orbital eccentricity led to an amplitude of SST variation of 0.7 – 0.8 ºC, 2–3 times higher than synchronous temperature variations recorded in the deep Atlantic Ocean. Compared to 100-kyr related variability in the tropical Atlantic (Fokkema et al. 2023), our amplitude suggests an amplification of this signal by a factor 3–4, much higher than previous early Eocene estimates of polar amplification of climate change. Importantly, by reconstructing the complete imprint of Milankovitch forcing on Arctic temperature variability, potential bias towards one end of the orbital climate variability can be excluded.

7. Acknowledgments

This work used samples retrieved by the International Ocean Discovery Program. We thank for Dr. H. Kuhlmann at Bremen Core Repository for providing the u-channels and core-catcher samples. We thank Antoinette van den Dikkenberg, Martin Luijendijk, Harvey de Graaf, Natasja Welters, Giovanni Dammers and Maxim Krasnoperov for their assistance in the lab and Lucas Lourens for discussions on the spectral analysis and tuning. We also thank the members of the ACEX scientific party. This work was funded by the European Research Council through Consolidator Grant 771497 awarded to AS under the Horizon 2020 program. This study benefitted from intellectual contributions by members of the Netherlands Earth System Science Centre, funded by Gravitation Grant 024.002.001 from the Dutch Ministry of Education, Culture and Science.

Open Research

All data presented in this work will be made openly available on zenodo.org.

References

Abbot, D. S., & Tziperman, E. (2008). Sea ice, high-latitude convection, and equable climates. Geophysical Research Letters, 35(3), 2007GL032286. ttps://doi.org/10.1029/2007GL032286

Abbot, Dorian S., & Tziperman, E. (2008). A high-latitude convective cloud feedback and equable climates. Quarterly Journal of the Royal Meteorological Society, 134(630), 165–185. https://doi.org/10.1002/qj.211

Anagnostou, E., John, E. H., Babila, T. L., Sexton, P. F., Ridgwell, A., Lunt, D. J., et al. (2020). Proxy evidence for state-dependence of climate sensitivity in the Eocene greenhouse. Nature Communications, 11(1), 4436. https://doi.org/10.1038/s41467-020-17887-x

Baatsen, M., Bijl, P., Von Der Heydt, A., Sluijs, A., & Dijkstra, H. (2024). Resilient Antarctic monsoonal climate prevented ice growth during the Eocene. Climate of the Past, 20(1), 77–90. https://doi.org/10.5194/cp-20-77-2024

Backman, J., Moran, K., McInroy, D. B., Mayer, L. A., & Expedition 302 Scientists (Eds.). (2006). Proceedings of the IODP, 302 (Vol. 302). Integrated Ocean Drilling Program. https://doi.org/10.2204/iodp.proc.302.2006

Barke, J., Abels, H. A., Sangiorgi, F., Greenwood, D. R., Sweet, A. R., Donders, T., et al. (2011). Orbitally forced Azolla blooms and Middle Eocene Arctic hydrology: Clues from palynology. Geology, 39(5), 427–430. https://doi.org/10.1130/G31640.1

Bijl, P. K., Schouten, S., Sluijs, A., Reichart, G.-J., Zachos, J. C., & Brinkhuis, H. (2009). Early Palaeogene temperature evolution of the southwest Pacific Ocean. Nature, 461(7265), 776–779. https://doi.org/10.1038/nature08399

Bijl, P. K., Frieling, J., Cramwinckel, M. J., Boschman, C., Sluijs, A., & Peterse, F. (2021). Maastrichtian–Rupelian paleoclimates in the southwest Pacific – a critical re-evaluation of biomarker paleothermometry and dinoflagellate cyst paleoecology at Ocean Drilling Program Site 1172. Climate of the Past, 17(6), 2393–2425. https://doi.org/10.5194/cp-17-2393-2021

Blaga, C. I., Reichart, G.-J., Heiri, O., & Sinninghe Damsté, J. S. (2009). Tetraether membrane lipid distributions in water-column particulate matter and sediments: a study of 47 European lakes along a north–south transect. Journal of Paleolimnology, 41(3), 523–540. https://doi.org/10.1007/s10933-008-9242-2

Browning, J. V., Miller, K. G., & Pak, D. K. (1996). Global implications of lower to middle Eocene sequence boundaries on the New Jersey coastal plain: The icehouse cometh. Geology, 24(7), 639. https://doi.org/10.1130/0091-7613(1996)024<0639:GIOLTM>2.3.CO;2

Carton, J. A., Ding, Y., & Arrigo, K. R. (2015). The seasonal cycle of the Arctic Ocean under climate change. Geophysical Research Letters, 42(18), 7681–7686. https://doi.org/10.1002/2015GL064514

Cramer, B. S., Wright, J. D., Kent, D. V., & Aubry, M.-P. (2003). Orbital climate forcing of D13C excursions in the late Paleocene—early Eocene (chrons C24n–C25n). Paleoceanography, 18, 1097. https://doi.org/10.1029/2003PA000909

Cramwinckel, M. J., Huber, M., Kocken, I. J., Agnini, C., Bijl, P. K., Bohaty, S. M., et al. (2018). Synchronous tropical and polar temperature evolution in the Eocene. Nature, 559(7714), 382–386. https://doi.org/10.1038/s41586-018-0272-2

Cramwinckel, M. J., Burls, N. J., Fahad, A. A., Knapp, S., West, C. K., Reichgelt, T., et al. (2023). Global and Zonal-Mean Hydrological Response to Early Eocene Warmth. Paleoceanography and Paleoclimatology, 38(6), e2022PA004542. https://doi.org/10.1029/2022PA004542

De Jonge, C., Hopmans, E. C., Zell, C. I., Kim, J.-H., Schouten, S., & Sinninghe Damsté, J. S. (2014). Occurrence and abundance of 6-methyl branched glycerol dialkyl glycerol tetraethers in soils: Implications for palaeoclimate reconstruction. Geochimica et Cosmochimica Acta, 141, 97–112. https://doi.org/10.1016/j.gca.2014.06.013

Dearing Crampton-Flood, E., Tierney, J. E., Peterse, F., Kirkels, F. M. S. A., & Sinninghe Damsté, J. S. (2020). BayMBT: A Bayesian calibration model for branched glycerol dialkyl glycerol tetraethers in soils and peats. Geochimica et Cosmochimica Acta, 268, 142–159. https://doi.org/10.1016/j.gca.2019.09.043

Dickens, G. R., O’Neil, J. R., Rea, D. K., & Owen, R. M. (1995). Dissociation of oceanic methane hydrate as a cause of the carbon isotope excursion at the end of the Paleocene. Paleoceanography, 10(6), 965–971. https://doi.org/10.1029/95PA02087

Dickens, G. R., Castillo, M. M., & Walker, J. C. G. (1997). A blast of gas in the latest Paleocene: Simulating first-order effects of massive dissociation of oceanic methane hydrate. Geology, 25(3), 259. https://doi.org/10.1130/0091-7613(1997)025<0259:ABOGIT>2.3.CO;2

Evans, D., Sagoo, N., Renema, W., Cotton, L. J., Müller, W., Todd, J. A., et al. (2018). Eocene greenhouse climate revealed by coupled clumped isotope-Mg/Ca thermometry. Proceedings of the National Academy of Sciences, 115(6), 1174–1179. https://doi.org/10.1073/pnas.1714744115

Fokkema, C. D., Agterhuis, T., Gerritsma, D., De Goeij, M., Liu, X., De Regt, P., et al. (2023). Polar amplification of orbital-scale climate variability in the early Eocene greenhouse world (Preprint). Climate of the Past Discussions. https://doi.org/10.5194/cp-2023-70

Frieling, J., & Sluijs, A. (2018). Towards quantitative environmental reconstructions from ancient non-analogue microfossil assemblages: Ecological preferences of Paleocene – Eocene dinoflagellates. Earth-Science Reviews, 185, 956–973. https://doi.org/10.1016/j.earscirev.2018.08.014

Galeotti, S., Krishnan, S., Pagani, M., Lanci, L., Gaudio, A., Zachos, J. C., et al. (2010). Orbital chronology of Early Eocene hyperthermals from the Contessa Road section, central Italy. Earth and Planetary Science Letters, 290(1–2), 192–200. https://doi.org/10.1016/j.epsl.2009.12.021

Ho, S. L., & Laepple, T. (2016). Flat meridional temperature gradient in the early Eocene in the subsurface rather than surface ocean. Nature Geoscience, 9(8), 606–610. https://doi.org/10.1038/ngeo2763

Hopmans, E. C., Weijers, J. W. H., Schefuß, E., Herfort, L., Sinninghe Damsté, J. S., & Schouten, S. (2004). A novel proxy for terrestrial organic matter in sediments based on branched and isoprenoid tetraether lipids. Earth and Planetary Science Letters, 224(1–2), 107–116. https://doi.org/10.1016/j.epsl.2004.05.012

Hopmans, E. C., Schouten, S., & Sinninghe Damsté, J. S. (2016). The effect of improved chromatography on GDGT-based palaeoproxies. Organic Geochemistry, 93, 1–6. https://doi.org/10.1016/j.orggeochem.2015.12.006

Hurley, S. J., Lipp, J. S., Close, H. G., Hinrichs, K.-U., & Pearson, A. (2018). Distribution and export of isoprenoid tetraether lipids in suspended particulate matter from the water column of the Western Atlantic Ocean. Organic Geochemistry, 116, 90–102. https://doi.org/10.1016/j.orggeochem.2017.11.010

Huybers, P. (2006). Early Pleistocene Glacial Cycles and the Integrated Summer Insolation Forcing. Science, 313(5786), 508–511. https://doi.org/10.1126/science.1125249

Inglis, G. N., Bragg, F., Burls, N. J., Cramwinckel, M. J., Evans, D., Foster, G. L., et al. (2020). Global mean surface temperature and climate sensitivity of the early Eocene Climatic Optimum (EECO), Paleocene–Eocene Thermal Maximum (PETM), and latest Paleocene. Climate of the Past, 16(5), 1953–1968. https://doi.org/10.5194/cp-16-1953-2020

Kennett, J. P., & Stott, L. D. (1991). Abrupt deep-sea warming, palaeoceanographic changes and benthic extinctions at the end of the Palaeocene. Nature, 353(6341), 225–229. https://doi.org/10.1038/353225a0

Kim, J.-H., van der Meer, J., Schouten, S., Helmke, P., Willmott, V., Sangiorgi, F., et al. (2010). New indices and calibrations derived from the distribution of crenarchaeal isoprenoid tetraether lipids: Implications for past sea surface temperature reconstructions. Geochimica et Cosmochimica Acta, 74(16), 4639–4654. https://doi.org/10.1016/j.gca.2010.05.027

Kindler, P., Guillevic, M., Baumgartner, M., Schwander, J., Landais, A., & Leuenberger, M. (2014). Temperature reconstruction from 10 to 120 kyr b2k from the NGRIP ice core. Climate of the Past, 10(2), 887–902. https://doi.org/10.5194/cp-10-887-2014

Kocken, I. J. (2022). colourlog: generate plots of colourlogs from core photographs. https://doi.org/10.5281/zenodo.7277860

Krishnan, S., Pagani, M., Huber, M., & Sluijs, A. (2014). High latitude hydrological changes during the Eocene Thermal Maximum 2. Earth and Planetary Science Letters, 404, 167–177. https://doi.org/10.1016/j.epsl.2014.07.029

Kutzbach, J. E., & Otto-Bliesner, B. L. (1982). The sensitivity of the African-Asian monsoonal climate to orbital parameter changes for 9000 years BP in a low-resolution general circulation model. Journal of Atmospheric Sciences, 39(6), 1177–1188.

Kutzbach, J. E., Liu, X., Liu, Z., & Chen, G. (2008). Simulation of the evolutionary response of global summer monsoons to orbital forcing over the past 280,000 years. Climate Dynamics, 30(6), 567–579. https://doi.org/10.1007/s00382-007-0308-z

Laskar, J., Robutel, P., Joutel, F., Gastineau, M., Correia, A. C. M., & Levrard, B. (2004). A long-term numerical solution for the insolation quantities of the Earth. Astronomy & Astrophysics, 428(1), 261–285. https://doi.org/10.1051/0004-6361:20041335

Laskar, J., Fienga, A., Gastineau, M., & Manche, H. (2011). La2010: a new orbital solution for the long-term motion of the Earth. Astronomy & Astrophysics, 532, A89. https://doi.org/10.1051/0004-6361/201116836

Lauretano, V., Zachos, J. C., & Lourens, L. J. (2018). Orbitally Paced Carbon and Deep-Sea Temperature Changes at the Peak of the Early Eocene Climatic Optimum. Paleoceanography and Paleoclimatology, 33(10), 1050–1065. https://doi.org/10.1029/2018PA003422

Li, M., Hinnov, L., & Kump, L. (2019). Acycle: Time-series analysis software for paleoclimate research and education. Computers & Geosciences, 127, 12–22. https://doi.org/10.1016/j.cageo.2019.02.011

Littler, K., Röhl, U., Westerhold, T., & Zachos, J. C. (2014). A high-resolution benthic stable-isotope record for the South Atlantic: Implications for orbital-scale changes in Late Paleocene–Early Eocene climate and carbon cycling. Earth and Planetary Science Letters, 401, 18–30. https://doi.org/10.1016/j.epsl.2014.05.054

Lourens, L. J., Sluijs, A., Kroon, D., Zachos, J. C., Thomas, E., Röhl, U., et al. (2005). Astronomical pacing of late Palaeocene to early Eocene global warming events. Nature, 435(7045), 1083–1087. https://doi.org/10.1038/nature03814

Lourens, L. J., Becker, J., Bintanja, R., Hilgen, F. J., Tuenter, E., Van De Wal, R. S. W., & Ziegler, M. (2010). Linear and non-linear response of late Neogene glacial cycles to obliquity forcing and implications for the Milankovitch theory. Quaternary Science Reviews, 29(1–2), 352–365. https://doi.org/10.1016/j.quascirev.2009.10.018

Loutre, M.-F., Paillard, D., Vimeux, F., & Cortijo, E. (2004). Does mean annual insolation have the potential to change the climate? Earth and Planetary Science Letters, 221(1–4), 1–14. https://doi.org/10.1016/S0012-821X(04)00108-6

Lunt, D. J., Bragg, F., Chan, W.-L., Hutchinson, D. K., Ladant, J.-B., Morozova, P., et al. (2021). DeepMIP: Model intercomparison of early Eocene climatic optimum (EECO) large-scale climate features and comparison with proxy data. Climate of the Past, 17, 203–227.

Martínez-Sosa, P., Tierney, J. E., Pérez-Angel, L. C., Stefanescu, I. C., Guo, J., Kirkels, F., et al. (2023). Development and Application of the Branched and Isoprenoid GDGT Machine Learning Classification Algorithm (BIGMaC) for Paleoenvironmental Reconstruction. Paleoceanography and Paleoclimatology, 38(7), e2023PA004611. https://doi.org/10.1029/2023PA004611

Massana, R., DeLong, E. F., & Pedrós-Alió, C. (2000). A Few Cosmopolitan Phylotypes Dominate Planktonic Archaeal Assemblages in Widely Different Oceanic Provinces. Applied and Environmental Microbiology, 66(5), 1777–1787. https://doi.org/10.1128/AEM.66.5.1777-1787.2000

Masson-Delmotte, V., Jouzel, J., Landais, A., Stievenard, M., Johnsen, S. J., White, J. W. C., et al. (2005). GRIP Deuterium Excess Reveals Rapid and Orbital-Scale Changes in Greenland Moisture Origin. Science, 309(5731), 118–121. https://doi.org/10.1126/science.1108575

Pagani, M., Pedentchouk, N., Huber, M., Sluijs, A., Schouten, S., Brinkhuis, H., et al. (2006). Arctic hydrology during global warming at the Palaeocene/Eocene thermal maximum. Nature, 442(7103), 671–675. https://doi.org/10.1038/nature05043

Pälike, H., Spofforth, D. J. A., O'Regan, M., & Gattacceca, J. (2008). Orbital scale variations and timescales from the Arctic Ocean. Paleoceanography, 23(1), PA1S10. https://doi.org/10.1029/2007PA001490

Peterse, F., Kim, J.-H., Schouten, S., Kristensen, D. K., Koç, N., & Sinninghe Damsté, J. S. (2009). Constraints on the application of the MBT/CBT palaeothermometer at high latitude environments (Svalbard, Norway). Organic Geochemistry, 40(6), 692–699. https://doi.org/10.1016/j.orggeochem.2009.03.004

Powell, A. J., Brinkhuis, H., & Bujak, J. P. (1996). Upper Paleocene-Lower Eocene dinoflagellate cyst sequence biostratigraphy of southeast England. Geological Society, London, Special Publications, 101(1), 145–183. https://doi.org/10.1144/GSL.SP.1996.101.01.10

Rattanasriampaipong, R., Zhang, Y. G., Pearson, A., Hedlund, B. P., & Zhang, S. (2022). Archaeal lipids trace ecology and evolution of marine ammonia-oxidizing archaea. Proceedings of the National Academy of Sciences, 119(31), e2123193119. https://doi.org/10.1073/pnas.2123193119

Raymo, M. E., & Nisancioglu, K. H. (2003). The 41 kyr world: Milankovitch's other unsolved mystery. Paleoceanography, 18(1), 2002PA000791. https://doi.org/10.1029/2002PA000791

Sangiorgi, F., van Soelen, E. E., Spofforth, D. J. A., Pälike, H., Stickley, C. E., St. John, K., et al. (2008). Cyclicity in the middle Eocene central Arctic Ocean sediment record: Orbital forcing and environmental response. Paleoceanography, 23(1). https://doi.org/10.1029/2007PA001487

Schouten, S., Hopmans, E. C., Schefuß, E., & Sinninghe Damsté, J. S. (2002). Distributional variations in marine crenarchaeotal membrane lipids: a new tool for reconstructing ancient sea water temperatures? Earth and Planetary Science Letters, 204(1–2), 265–274. https://doi.org/10.1016/S0012-821X(02)00979-2

Schubert, B. A., Jahren, A. H., Eberle, J. J., Sternberg, L. S. L., & Eberth, D. A. (2012). A summertime rainy season in the Arctic forests of the Eocene. Geology, 40(6), 523–526. https://doi.org/10.1130/G32856.1

Sinninghe Damsté, J. S. (2016). Spatial heterogeneity of sources of branched tetraethers in shelf systems: The geochemistry of tetraethers in the Berau River delta (Kalimantan, Indonesia). Geochimica et Cosmochimica Acta, 186, 13–31. https://doi.org/10.1016/j.gca.2016.04.033

Sinninghe Damsté, J. S., Rijpstra, W. I. C., Hopmans, E. C., Prahl, F. G., Wakeham, S. G., & Schouten, S. (2002). Distribution of Membrane Lipids of Planktonic Crenarchaeota in the Arabian Sea. Applied and Environmental Microbiology, 68(6), 2997–3002. https://doi.org/10.1128/AEM.68.6.2997-3002.2002

Sluijs, A., & Brinkhuis, H. (2009). A dynamic climate and ecosystem state during the Paleocene-Eocene Thermal Maximum: inferences from dinoflagellate cyst assemblages on the New Jersey Shelf. Biogeosciences, 6(8), 1755–1781. https://doi.org/10.5194/bg-6-1755-2009

Sluijs, Appy, Schouten, S., Pagani, M., Woltering, M., Brinkhuis, H., Damsté, J. S. S., et al. (2006). Subtropical Arctic Ocean temperatures during the Palaeocene/Eocene thermal maximum. Nature, 441(7093), 610–613. https://doi.org/10.1038/nature04668

Sluijs, Appy, Röhl, U., Schouten, S., Brumsack, H.-J., Sangiorgi, F., Sinninghe Damsté, J. S., & Brinkhuis, H. (2008). Arctic late Paleocene-early Eocene paleoenvironments with special emphasis on the Paleocene-Eocene thermal maximum (Lomonosov Ridge, Integrated Ocean Drilling Program Expedition 302). Paleoceanography, 23(1),PA1S11. https://doi.org/10.1029/2007PA001495

Sluijs, Appy, Brinkhuis, H., Crouch, E. M., John, C. M., Handley, L., Munsterman, D., et al. (2008). Eustatic variations during the Paleocene-Eocene greenhouse world. Paleoceanography, 23(4), PA4216. https://doi.org/10.1029/2008PA001615

Sluijs, Appy, Schouten, S., Donders, T. H., Schoon, P. L., Röhl, U., Reichart, G.-J., et al. (2009). Warm and wet conditions in the Arctic region during Eocene Thermal Maximum 2. Nature Geoscience, 2(11), 777–780. https://doi.org/10.1038/ngeo668

Sluijs, Appy, Frieling, J., Inglis, G. N., Nierop, K. G. J., Peterse, F., Sangiorgi, F., & Schouten, S. (2020). Late Paleocene–early Eocene Arctic Ocean sea surface temperatures: reassessing biomarker paleothermometry at Lomonosov Ridge. Climate of the Past, 16(6), 2381–2400. https://doi.org/10.5194/cp-16-2381-2020

Speelman, E. N., Sewall, J. O., Noone, D., Huber, M., Der Heydt, A. V., Damsté, J. S., & Reichart, G.-J. (2010). Modeling the influence of a reduced equator-to-pole sea surface temperature gradient on the distribution of water isotopes in the Early/Middle Eocene. Earth and Planetary Science Letters, 298(1–2), 57–65. https://doi.org/10.1016/j.epsl.2010.07.026

Stap, L., Lourens, L. J., Thomas, E., Sluijs, A., Bohaty, S., & Zachos, J. C. (2010). High-resolution deep-sea carbon and oxygen isotope records of Eocene Thermal Maximum 2 and H2. Geology, 38(7), 607–610. https://doi.org/10.1130/G30777.1

Stein, R., Boucsein, B., & Meyer, H. (2006). Anoxia and high primary production in the Paleogene central Arctic Ocean: First detailed records from Lomonosov Ridge. Geophysical Research Letters, 33(18). https://doi.org/10.1029/2006GL026776

Suan, G., Popescu, S.-M., Suc, J.-P., Schnyder, J., Fauquette, S., Baudin, F., et al. (2017). Subtropical climate conditions and mangrove growth in Arctic Siberia during the early Eocene. Geology, 45(6), 539–542. https://doi.org/10.1130/G38547.1

Taylor, K. W. R., Huber, M., Hollis, C. J., Hernandez-Sanchez, M. T., & Pancost, R. D. (2013). Re-evaluating modern and Palaeogene GDGT distributions: Implications for SST reconstructions. Global and Planetary Change, 108, 158–174. https://doi.org/10.1016/j.gloplacha.2013.06.011

Uemura, R., Motoyama, H., Masson-Delmotte, V., Jouzel, J., Kawamura, K., Goto-Azuma, K., et al. (2018). Asynchrony between Antarctic temperature and CO2 associated with obliquity over the past 720,000 years. Nature Communications, 9(1), 961. https://doi.org/10.1038/s41467-018-03328-3

Varma, D., Hättig, K., Van Der Meer, M. T. J., Reichart, G., & Schouten, S. (2023). Constraining Water Depth Influence on Organic Paleotemperature Proxies Using Sedimentary Archives. Paleoceanography and Paleoclimatology, 38(6), e2022PA004533. https://doi.org/10.1029/2022PA004533

Vimeux, F., Masson, V., Delaygue, G., Jouzel, J., Petit, J. R., & Stievenard, M. (2001). A 420,000 year deuterium excess record from East Antarctica: Information on past changes in the origin of precipitation at Vostok. Journal of Geophysical Research: Atmospheres, 106(D23), 31863–31873. https://doi.org/10.1029/2001JD900076

Weijers, J. W. H., Schouten, S., Spaargaren, O. C., & Sinninghe Damsté, J. S. (2006). Occurrence and distribution of tetraether membrane lipids in soils: Implications for the use of the TEX86 proxy and the BIT index. Organic Geochemistry, 37(12), 1680–1693. https://doi.org/10.1016/j.orggeochem.2006.07.018

Weijers, J. W. H., Schouten, S., Van Den Donker, J. C., Hopmans, E. C., & Sinninghe Damsté, J. S. (2007). Environmental controls on bacterial tetraether membrane lipid distribution in soils. Geochimica et Cosmochimica Acta, 71(3), 703–713. https://doi.org/10.1016/j.gca.2006.10.003

Weijers, J. W. H., Lim, K. L. H., Aquilina, A., Sinninghe Damsté, J. S., & Pancost, R. D. (2011). Biogeochemical controls on glycerol dialkyl glycerol tetraether lipid distributions in sediments characterized by diffusive methane flux. Geochemistry, Geophysics, Geosystems, 12(10), Q10010. https://doi.org/10.1029/2011GC003724

van der Weijst, C. M. H., van der Laan, K. J., Peterse, F., Reichart, G.-J., Sangiorgi, F., Schouten, S., et al. (2022). A 15-million-year surface- and subsurface-integrated TEX86 temperature record from the eastern equatorial Atlantic. Climate of the Past, 18(8), 1947–1962. https://doi.org/10.5194/cp-18-1947-2022

West, C. K., Greenwood, D. R., & Basinger, J. F. (2015). Was the Arctic Eocene ‘rainforest’ monsoonal? Estimates of seasonal precipitation from early Eocene megafloras from Ellesmere Island, Nunavut. Earth and Planetary Science Letters, 427, 18–30. https://doi.org/10.1016/j.epsl.2015.06.036

Westerhold, T., Röhl, U., Pälike, H., Wilkens, R., Wilson, P. A., & Acton, G. (2014). Orbitally tuned timescale and astronomical forcing in the middle Eocene to early Oligocene. Climate of the Past, 10(3), 955–973. https://doi.org/10.5194/cp-10-955-2014

Westerhold, T., Röhl, U., Donner, B., & Zachos, J. C. (2018). Global Extent of Early Eocene Hyperthermal Events: A New Pacific Benthic Foraminiferal Isotope Record From Shatsky Rise (ODP Site 1209). Paleoceanography and Paleoclimatology, 33(6), 626–642. https://doi.org/10.1029/2017PA003306

Westerhold, Thomas, Röhl, U., Frederichs, T., Agnini, C., Raffi, I., Zachos, J. C., & Wilkens, R. H. (2017). Astronomical calibration of the Ypresian timescale: implications for seafloor spreading rates and the chaotic behavior of the solar system? Climate of the Past, 13(9), 1129–1152. https://doi.org/10.5194/cp-13-1129-2017

Westerhold, Thomas, Marwan, N., Drury, A. J., Liebrand, D., Agnini, C., Anagnostou, E., et al. (2020). An astronomically dated record of Earth’s climate and its predictability over the last 66 million years. Science, 369(6509), 1383–1387. https://doi.org/10.1126/science.aba6853

Willard, D. A., Donders, T. H., Reichgelt, T., Greenwood, D. R., Sangiorgi, F., Peterse, F., et al. (2019). Arctic vegetation, temperature, and hydrology during Early Eocene transient global warming events. Global and Planetary Change, 178, 139–152. https://doi.org/10.1016/j.gloplacha.2019.04.012

Xiao, W., Wang, Y., Zhou, S., Hu, L., Yang, H., & Xu, Y. (2016). Ubiquitous production of branched glycerol dialkyl glycerol tetraethers(brGDGTs) in global marine environments: a new source indicator for brGDGTs. Biogeosciences, 13(20), 5883–5894. https://doi.org/10.5194/bg-13-5883-2016

Xiao, W., Wang, Y., Liu, Y., Zhang, X., Shi, L., & Xu, Y. (2020). Predominance of hexamethylated 6-methyl branched glycerol dialkyl glycerol tetraethers in the Mariana Trench: source and environmental implication. Biogeosciences, 17(7), 2135–2148. https://doi.org/10.5194/bg-17-2135-2020

Zachos, J. C., Wara, M. W., Bohaty, S., Delaney, M. L., Petrizzo, M. R., Brill, A., et al. (2003). A Transient Rise in Tropical Sea Surface Temperature During the Paleocene-Eocene Thermal Maximum. Science, 302(5650), 1551–1554. https://doi.org/10.1126/science.1090110

Zeebe, R. E., & Lourens, L. J. (2019). Solar System chaos and the Paleocene–Eocene boundary age constrained by geology and astronomy. Science, 365(6456), 926–929. https://doi.org/10.1126/science.aax0612

Zeeden, C., Hilgen, F., Röhl, U., Seelos, K., & Lourens, L. (2015). Sediment color as a tool in cyclostratigraphy – a new application for improved data acquisition and correction from drill cores. Newsletters on Stratigraphy, 48(3), 277–285. https://doi.org/10.1127/nos/2015/0064

Zell, C., Kim, J.-H., Moreira-Turcq, P., Abril, G., Hopmans, E. C., Bonnet, M.-P., et al. (2013). Disentangling the origins of branched tetraether lipids and crenarchaeol in the lower Amazon River: Implications for GDGT-based proxies. Limnology and Oceanography, 58(1), 343–353. https://doi.org/10.4319/lo.2013.58.1.0343

Zhang, Y. G., Zhang, C. L., Liu, X.-L., Li, L., Hinrichs, K.-U., & Noakes, J. E. (2011). Methane Index: A tetraether archaeal lipid biomarker indicator for detecting the instability of marine gas hydrates. Earth and Planetary Science Letters, 307(3–4), 525–534. https://doi.org/10.1016/j.epsl.2011.05.031

Zhang, Y. G., Pagani, M., & Wang, Z. (2016). Ring Index: A new strategy to evaluate the integrity of TEX 86 paleothermometry. Paleoceanography, 31(2), 220–232. https://doi.org/10.1002/2015PA002848